Geoscientific
Model Development

Development and evaluation of CNRM Earth system model – CNRM-ESM1

Roland Séférian[1], **Christine Delire**[1], **Bertrand Decharme**[1], **Aurore Voldoire**[1], **David Salas y Melia**[1],
Matthieu Chevallier[1], **David Saint-Martin**[1], **Olivier Aumont**[2], **Jean-Christophe Calvet**[1], **Dominique Carrer**[1],
Hervé Douville[1], **Laurent Franchistéguy**[1], **Emilie Joetzjer**[3], and **Séphane Sénési**[1]

[1]CNRM, Centre National de Recherches Météorologiques, Météo-France/CNRS, 42 Avenue Gaspard Coriolis,
31057 Toulouse, France
[2]Sorbonne Universités (UPMC, Univ Paris 06)-CNRS-IRD-MNHN, LOCEAN-IPSL Laboratory, 4 Place Jussieu,
75005 Paris, France
[3]Department of Ecology, Institute on Ecosystems, Montana State University, 111 AJM Johnson Hall, Bozeman,
Montana 59717, USA

Correspondence to: Roland Séférian (rseferian.cnrm@gmail.com)

Abstract. We document the first version of the Centre National de Recherches Météorologiques Earth system model (CNRM-ESM1). This model is based on the physical core of the CNRM climate model version 5 (CNRM-CM5) model and employs the Interactions between Soil, Biosphere and Atmosphere (ISBA) and the Pelagic Interaction Scheme for Carbon and Ecosystem Studies (PISCES) as terrestrial and oceanic components of the global carbon cycle. We describe a preindustrial and 20th century climate simulation following the CMIP5 protocol. We detail how the various carbon reservoirs were initialized and analyze the behavior of the carbon cycle and its prominent physical drivers. Over the 1986–2005 period, CNRM-ESM1 reproduces satisfactorily several aspects of the modern carbon cycle. On land, the model captures the carbon cycling through vegetation and soil, resulting in a net terrestrial carbon sink of $2.2\,\mathrm{Pg\,C\,year^{-1}}$. In the ocean, the large-scale distribution of hydrodynamical and biogeochemical tracers agrees with a modern climatology from the World Ocean Atlas. The combination of biological and physical processes induces a net CO_2 uptake of $1.7\,\mathrm{Pg\,C\,year^{-1}}$ that falls within the range of recent estimates. Our analysis shows that the atmospheric climate of CNRM-ESM1 compares well with that of CNRM-CM5. Biases in precipitation and shortwave radiation over the tropics generate errors in gross primary productivity and ecosystem respiration. Compared to CNRM-CM5, the revised ocean–sea ice coupling has modified the sea-ice cover and ocean ventilation, unrealistically strengthening the flow of North Atlantic deep water (26.1 ± 2 Sv). It results in an accumulation of anthropogenic carbon in the deep ocean.

1 Introduction

Earth system models (ESMs) are now recognized as the current state-of-the-art models (IPCC, 2013), expanding the numerical representation of the climate system of the 4th Assessment Report (IPCC, 2007). They enable the representation of subtle nonlinear interactions and feedbacks of different magnitude and signs of various biogeochemical and biophysical processes with the climate system. The latter contribute, in addition to the atmospheric radiative properties and global climate dynamics, to determining the Earth's climate variability (Arora et al., 2013; Cox et al., 2000; Friedlingstein and Prentice, 2010; Schwinger et al., 2014; Wetzel et al., 2006).

Although there is no uniformly accepted definition, ESMs generally bring together a global physical climate model and land and ocean biogeochemical modules (Bretherton, 1985; Flato, 2011). As such, they enable the representation of the global carbon cycle. The models of this class have played a larger role in the 5th IPCC report than in previous reports,

primarily through their contribution to the concentration- and emission-driven experiments that compose CMIP5.

Even if the concept of Earth system modeling is being extended to include further processes and reservoirs (e.g., nitrogen cycle, aerosols) (Hajima et al., 2014), there are still large uncertainties in the representation of the carbon cycle and its interactions with climate (Anav et al., 2013a; Friedlingstein et al., 2013; Piao et al., 2013). To reduce them, there is a need for improvements of both physical and ecophysiological parameterizations (Dalmonech et al., 2014), and for the development of observation-based methods to constrain model projections (Wenzel et al., 2014). But the reduction of carbon cycle–climate uncertainties also requires a greater number and diversity of ESMs. This path is promoted and followed by various international initiatives like the Global Carbon Budget (http://www.globalcarbonproject.org/) that sequentially incorporate more and more models into their analyses (Le Quéré et al., 2013, 2015).

This article documents the first IPCC-class ESM developed at Centre National de Recherches Météorologiques (CNRM) and provides a basic evaluation of the model's skill. This model is based on the CNRM-CM5.1 climate model jointly developed by CNRM and Cerfacs (Centre Européen de Recherche et de Formation Avancée en Calcul Scientifique), which has contributed to the 5th phase of the Coupled Model Intercomparison Project (CMIP5) (Voldoire et al., 2013). CNRM-CM5.1 did not include a representation of the global carbon cycle but accounted for chemical–climate interactions with an interactive stratospheric chemistry module (Cariolle and Teyssèdre, 2007). While this configuration of CNRM-CM5 contributed to the CMIP5 results publicly released, a first intermediate version of the CNRM ESM was developed with the inclusion of the marine biogeochemistry model Pelagic Interaction Scheme for Carbon and Ecosystem Studies (PISCES) (Aumont and Bopp, 2006). This model version was evaluated against modern oceanic observations (Séférian et al., 2013) and employed in various studies (Frölicher et al., 2014; Laufkötter et al., 2015; Schwinger et al., 2014; Séférian et al., 2014).

A terrestrial carbon cycle module has been under development at CNRM since the 2000s (Calvet and Soussana, 2001; Calvet et al., 2008, 2004; Gibelin et al., 2008, 2006), but it has never been coupled to an atmosphere–ocean model. This carbon cycle module evolved from the physically based Interactions between Soil, Biosphere and Atmosphere (ISBA) model (Noilhan and Mahfouf, 1996; Noilhan and Planton, 1989) and is able to simulate the surface carbon fluxes and the terrestrial carbon pools. The carbon fluxes module was extensively tested over France and Europe (Sarrat et al., 2007; Szczypta et al., 2012), and the carbon cycle module was tested for temperate and high-latitude regions (Gibelin et al., 2006, 2008) and was used more recently in studies of carbon cycling over the Amazon basin (Joetzjer et al., 2015, 2014), permafrost regions (Rawlins et al., 2015) and at global scale (Carrer et al., 2013b). In this work, this terrestrial car-

bon cycle module is coupled to a global climate model for the first time.

Here, we present a first evaluation of the CNRM-ESM1. In Sect. 2, we describe the model, focusing on the Earth system's components and aspects of the climate model that are particularly relevant to the global carbon cycle. We describe in Sect. 3 the preindustrial control and 20th century experiments that we conducted, together with the forcings used and how the experiments were initialized. In Sect. 4, we present and discuss the results of these experiments. We summarize the results in Sect. 5 and present conclusions.

2 CNRM-ESM components

2.1 The physical core

CNRM-ESM1 is based on the physical core of the CNRM-CM5.1 atmosphere–ocean general circulation model extensively described in Voldoire et al. (2013), which accounts for the physical and dynamical interactions occurring between atmosphere, land, ocean and sea ice.

The atmospheric component is based on version 6.1 of the global spectral model ARPEGE-Climat, which corresponds to an updated version of the atmospheric code used in CNRM-CM5.1. This updated version of the atmospheric code is derived from cycle 37 of the ARPEGE-IFS (integrated forecast system) numerical weather prediction model developed jointly by Météo-France and the European Center for Medium-range Weather Forecast. In CNRM-ESM1, the geometry, parameterizations and dynamics have been chosen to match the choices made for CNRM-CM5.1. Thus, differences are mainly due to debugging and recoding. The atmospheric physics and dynamics are solved on a T127 triangular truncation that offers a spatial resolution of about 1.4° in both longitude and latitude. Consistent with CNRM-CM5.1, CNRM-ESM1 employs a "low-top" configuration with 31 vertical levels that extend from the surface to 10 hPa in the stratosphere. The layers are unevenly distributed with six layers below 850 hPa except in regions of high orography, nine layers above 200 hPa and four layers above 100 hPa. The dynamical core of the model, the radiative scheme for longwave and shortwave, as well as the physical parameterization for deep and shallow convection, are identical to those employed in CNRM-CM5.1. The reader is referred to Voldoire et al. (2013) for the original description of the atmospheric model parameterizations.

The land-surface component is an updated version of the SURFface EXternalisée modeling platform (SURFEXv7.3) (Masson et al., 2013b) associated with the total runoff integrating pathways (TRIP) river routing model (Oki and Sud, 1997). SURFEX was designed so that the same code could be run offline or coupled to a general circulation model (GCM), allowing for easy transfer from offline improvements to the

coupled model and to be able to compare online and offline runs.

This model prognostically computes the exchange of energy, water and carbon between the atmosphere and three types of natural surfaces: land, free water bodies and oceans or seas. The energy, water and carbon balances are calculated separately for each surface type and area averaged over each atmospheric grid cell. The natural land surfaces are represented by the module originally developed by Noilhan and Planton (1989). This module solves the surface energy and soil water budgets using the force–restore method and a composite soil–vegetation–snow approach. The version used here is the same as for CNRM-CM5.1; e.g., the soil hydrology uses three vertical layers (Boone et al., 1999) while soil temperature is solved using four vertical layers. In CNRM-ESM1, land-surface albedo benefits from an improved spatial representation derived from MODIS satellite measurements (Carrer et al., 2013a) except for the area covered by snow for which the albedo is prognostically computed following Douville et al. (1995). Over water bodies and oceans, we use the CNRM-CM5.1 parameterization for momentum and energy fluxes except for the sea-to-air turbulent fluxes that are computed from the Coupled Ocean–Atmosphere Response Experiment (COARE) scheme (Fairall et al., 2003). Interactions between the land-surface energy and water budgets and the terrestrial carbon cycle module are detailed in Sect. 2.3.1.

The ocean component uses version 3.2 of the Nucleus for European Modelling of the Ocean (NEMO) model (Madec, 2008) in the ORCA1L42 configuration. This configuration offers a horizontal resolution from 1 to $1/3°$ near the Equator and 42 levels in depth. The vertical discretization uses a partial-step formulation (Barnier et al., 2006), which ensures a better representation of bottom bathymetry and thus streamflow and friction at the bottom of the ocean. Ocean dynamics and physics is solved using a time step of 1 h. Vertical physics relies on the parameterization chosen for the CNRM-CM5.1 climate model. The mixed-layer dynamics is parameterized using a double diffusion process (Merryfield et al., 1999), Langmuir cell (Axell, 2002) and account for the contribution of surface wave breaking (Mellor and Blumberg, 2004). A parameterization of bottom intensified tidal-driven mixing similar to Simmons et al. (2004) is used in combination with a specific tidal mixing parameterization in the Indonesian area (Koch-Larrouy et al., 2010, 2007). Finally, CNRM-ESM1 benefits from an improved turbulent kinetic energy (TKE) closure scheme (Madec, 2008), based on the Blanke and Delecluse (1993) TKE. This parameterization allows for a fraction of surface wind energy to penetrate below the base of the mixed layer ensuring a better coupling between surface wind and subsurface mixing. The main difference of the CNRM-CM5.1 ocean model is the explicit modulation of the radiative shortwave penetration into the ocean by marine biota (Lengaigne et al., 2009; Mignot et al., 2013), which is further detailed in Sect. 2.3.2.

The sea-ice model used in CNRM-ESM1 is Global Experimental Leads and ice for ATmosphere and Ocean (GELATO6). This model employs the same horizontal grid as NEMO and solves sea-ice dynamics and thermodynamics every 6 h. This model represents an updated version of the former sea-ice model used in CNRM-CM5.1 (Voldoire et al., 2013). In GELATO6, sea-ice dynamics is computed using the elastic viscous–plastic scheme proposed by Hunke and Dukowicz (1997) formulated on an Arakawa C-grid (Bouillon et al., 2009). To simulate the response of sea ice to convergence–divergence movements, GELATO6 employs a redistribution scheme derived from Thorndike et al. (1975). This scheme ensures the representation of the rafting phenomenon for the slab of sea ice thinner than 0.25 m and of ridging for the slab thicker than 0.25 m. GELATO6 includes a thermodynamic scheme that resolves the evolution of four ice thickness categories (0–0.3, 0.3–0.8, 0.8–3 and over 3 m). These four slabs of sea ice are modeled with 10 vertical layers unevenly distributed across the slab thickness. An enhanced resolution at the top of the slab is used to better represent the evolution of sea ice in response to the high-frequency variability of the atmospheric thermal forcing. Besides, all sea-ice slabs may be covered with one snow layer. In GELATO6, the snow layer is considered to occult the transfer of light across the snow–sea ice–ocean continuum. This snow layer can age or form ice using the formulation described in Salas y Mélia (2002). Since CNRM-CM5.1, the coupling between NEMO and GELATO has been revised in order to improve the conservation of water and salt. In the previous model version, CNRM-CM5.1, there was a large drift in salinity (-0.011 psu century^{-1}) and in sea level (-21 cm century^{-1}). These were caused by (1) the melting of land glaciers (other than Antarctic and Greenland) that was not routed to the ocean and (2) an erroneous coupling between sea-ice and ocean models. The coupling did not take into account the fact that sea ice is levitating over the ocean in this version of NEMO. Although not severe, it resulted in a loss of water in the model. These errors have been fixed in CNRM-CM5-2 and CNRM-ESM1 and hence reducing the residual drifts in salinity to $+0.001$ psu century^{-1} and in sea level to $+1.2$ cm century^{-1}.

In CNRM-ESM1, exchanges of momentum, water and energy between the atmosphere and the surface models occurs every atmospheric time step (i.e., 30 min) because SURFEX is a submodel of the atmospheric code. The coupling between the atmosphere and the ocean models is handled by the OASIS coupler (Valcke, 2013) and occurs every 6 h. In CNRM-ESM1, the frequency of coupling between the ocean and atmosphere models has been increased compared to CNRM-CM5 in order to better resolve the dynamics of the sea ice, which is resolved at this time step (i.e., 6 h).

2.2 Atmospheric chemistry

The atmospheric chemistry scheme in CNRM-ESM1 consists of an interactive linear ozone chemistry performed with the MOdèle BIDImensionnel de Chimie (MOBIDIC, Cariolle and Teyssèdre, 2007) including a representation of the three-dimensional atmospheric CO_2 mixing ratio.

As in CNRM-CM5, the ozone mixing ratio is treated as a prognostic variable with photochemical production and loss rates climatology computed by a full chemistry scheme. That is, the net photochemical production in the ozone continuity equation is solved using a first-order Taylor series around the local value of the ozone mixing ratio, air temperature and the overhead ozone column. Ozone destruction terms are used to parameterize the heterogeneous chemistry as a function of the equivalent chlorine content prescribed for the actual year. All Taylor coefficients of this linearized scheme were determined using a two-dimensional chemistry scheme with 56 constituents, 175 chemical reactions, and 51 photoreactions (Cariolle and Brard, 1985). Photochemical production and loss rates of ozone rely on the main gas-phase reactions driving the NO_x, HO_x, ClO_x, BrO_x catalytic cycles. In this version, the gas-phase chemical rates were upgraded according to the recommendations of Sander et al. (2006). While the ozone mixing ratio is fully described across the atmospheric column, the linear ozone scheme was especially designed to resolve its evolution in the stratosphere for the sake of radiative transfer calculation. Therefore, some tropospheric chemical reactions are not taken into account in this scheme. The reader is referred to an article by Eyring et al. (2013) for an extensive evaluation of the linear scheme vs. the Total Ozone Mapping Spectrometer (TOMS) satellite measurements and intercomparison with other CMIP5 models.

In CNRM-ESM1, the atmospheric CO_2 mixing ratio can be treated as a prognostic tracer. It responds interactively to natural CO_2 exchange from land and ocean every 30 min and 6 h, respectively, while anthropogenic carbon emissions are prescribed in this model version. The CO_2 mixing ratio can affect the physical climate by impacting the atmospheric radiative transfer computations and both terrestrial and marine carbon uptake. In the concentration-driven experiments presented here, the CO_2 mixing ratio is, however, prescribed to the global yearly average atmospheric concentrations according to the CMIP5 protocol.

2.3 The biogeochemical components

2.3.1 Land biogeochemical model

In CNRM-ESM1, the interactions between climate and vegetation are handled by the ISBA scheme embedded in the SURFEX (Surface Externalisée) model. The land biogeochemical module in ISBA represents land-surface physics, plant physiology, carbon allocation and turnover, and carbon cycling through litter and soil (Calvet and Soussana, 2001;

Calvet et al., 1998; Gibelin et al., 2006, 2008). The land cover is represented by nine plant functional types (PFT; given in Fig. 1) and three non-vegetated surface types that are determined spatially by the ECOCLIMAP physiographic database (Masson et al., 2013a).

ISBA uses a semi-mechanistic treatment of canopy photosynthesis and mesophyll conductance following the Jacobs et al. (1996) and Goudriaan et al. (1985) photosynthesis model. Mesophyll conductance in this framework corresponds to the rate of photosynthesis under light-saturated conditions (Jacobs et al., 1996). As such, this scheme does not explicitly account for Michaelis–Menten kinetics of the Rubisco enzyme found in Farquhar et al. (1980) and Collatz et al. (1992) models. ISBA includes a representation of the soil water stress. Key parameters of the photosynthesis model respond to the soil water stress, permitting the representation of drought-avoiding and drought-tolerant responses to drought. For low vegetation and for trees, the response to drought is based on the meta-analyses of Calvet (2000) and Calvet et al. (2004), respectively.

The model simulates a ratio of intercellular CO_2 to atmospheric CO_2 that depends on leaf-to-air saturation deficit, leaf temperature and soil moisture. Assimilation is calculated from this ratio, air CO_2 concentration, leaf temperature and solar radiation considering plant photosynthetic pathways: C_3 or C_4 (Calvet et al., 1998; Gibelin et al., 2006). Stomatal conductance, which represents the vegetation control on gas transfer (here, CO_2 and water vapor) between the leaves and the atmosphere, is finally deduced from the assimilation rate. Leaf dark respiration is taken as a fraction of maximum CO_2 limited rate of assimilation. Standard Q_{10} response functions determine the temperature dependencies of mesophyll conductance, CO_2 compensation point, maximum photosynthetic rate and, hence, photosynthesis and respiration.

ISBA simulates the evolution of six reservoirs of biomass including leaf, wood and roots, and assumes the existence of metabolic/structural reservoirs of biomass (Gibelin et al., 2008). Vegetation biomass is simulated interactively based on the carbon assimilated by photosynthesis, and decreased by turnover and respiration. The autotrophic respiration combines the respiration from all these reservoirs except the woody reservoir that is supposed not to respire (Gibelin et al., 2008). In this model, the vegetation phenology results directly from the carbon balance of the leaves. Therefore, phenology is completely driven by photosynthesis and no growing degree-day model is used. A key advantage of this approach is that most of the soil and atmospheric drivers (the abiotic drivers) of phenology are accounted for without any additional parameters (Szczypta et al., 2014). Leaf area index (LAI) is determined from the leaf biomass and the specific leaf area index, which varies as a function of leaf nitrogen concentration and plant functional type (Gibelin et al., 2006). ISBA uses an implicit nitrogen limitation parameterization, which is based on the meta-analysis of leaf nitrogen measurement under CO_2 enrichment condition (Yin et al.,
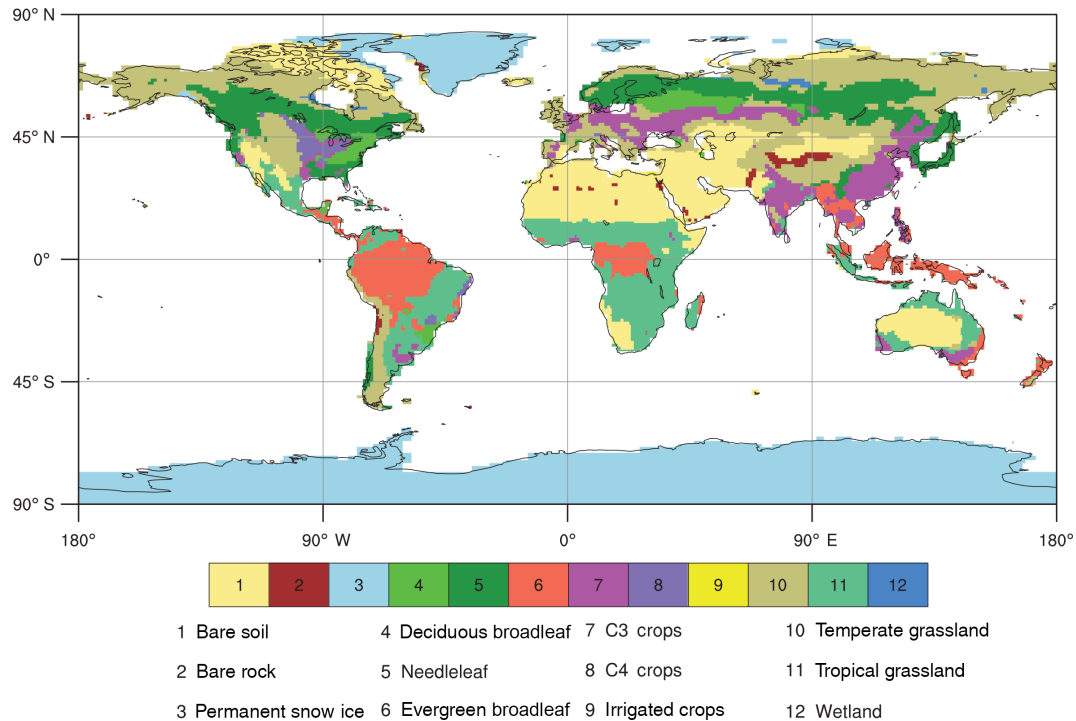
Figure 1. Fraction of dominant vegetation type as prescribed in SURFEX. This fraction results from aggregation of the various ECO-CLIMAP's vegetation types at 1 km resolution over the T127 CNRM-ESM1 horizontal grid ($\sim 1.4°$ nominal horizontal resolution).

2002). This simple implicit nitrogen limitation is based on the nitrogen dilution hypothesis, which assumes that internal nitrogen content of a plant decrease under rising CO_2 due to the accumulation of non-structural carbohydrates. It results that nitrogen dilution occurs as soon as the increase in total biomass of a plant under rising CO_2 relative to growth under ambient CO_2 is greater than the corresponding increase in total nitrogen. In current version of ISBA, a linear decrease between specific leaf area index and nitrogen to carbon ratio in leaves is used to mimic this mechanism (Calvet et al., 2008), and hence to limit the net assimilation of atmospheric CO_2.

The soil organic matter and litter module in ISBA follows the soil carbon part of the CENTURY model (Parton et al., 1988). Four pools of litter are represented. They are differentiated by their location above- or belowground and their content of lignin. The litter pools are supplied by the fluxes of dead biomass from each biomass reservoir (turnover) as described in Gibelin et al. (2008). The three soil organic matter reservoirs (active, slow and passive) are characterized by their resistance to decomposition with turnover times spanning from a few months for the active pool to 240 years for the passive pool. Heterotrophic respiration and hence the flux of CO_2 released to the atmosphere is the sum of respiration from the litter and soil organic matter reservoirs. The rate of decomposition of organic matter is determined essentially by soil moisture and temperature using a Q_{10} dependence

following the formulation of Krinner et al. (2005). The rate of decomposition (by respiration) depends also on the lignin fraction and the soil texture following Parton et al. (1988).

Changes in the carbon balance of the vegetation affect the energy and water balance, and hence the climate, through changes in stomatal conductance and LAI. Through its control on leaf transpiration, stomatal conductance affects latent heat flux and the surface energy balance. LAI on the other hand affects evapotranspiration because it is used to scale leaf-level to canopy-level transpiration and evaporation from the interception reservoir (water intercepted by leaves).

In CNRM-ESM1, except for crops, changes in LAI do not affect the albedo of the land surface, as it is the case in some other models. As mentioned earlier, albedo is derived from satellite observations corrected in the presence of snow, but does not depend on the changes in LAI calculated by the model. This limits the biophysical feedback from vegetation change to the atmosphere.

2.3.2 Ocean biogeochemical model

The ocean biogeochemical model of CNRM-ESM1 is PISCES (Aumont and Bopp, 2006). This model simulates the biogeochemical cycles of oxygen, carbon and the main nutrients with 24 state variables. Macronutrients (i.e., nitrate and ammonium, phosphate, silicate) and micronutrients (i.e., iron) ensure a better representation of the phytoplankton dynamics, because these five nutrients contribute to the nutri-

ent limitation process (Aumont et al., 2003). PISCES represents two size classes of phytoplankton (i.e., nanophytoplankton and diatoms). Dependence of growth on temperature is parameterized according to Eppley et al. (1969). Growth rate is also limited by the external availability in nutrients using the Michaelis–Menten relationships. Diatoms differ from nanophytoplankton by their need in silicon, by higher requirements in iron (Sunda and Huntsman, 1997) and by higher half-saturation constants because of their larger mean surface-to-volume aspect ratio. Zooplankton is represented by two size classes: microzooplankton and mesozooplankton.

PISCES can be considered as a Monod model (Monod, 1942) since it does not represent the internal concentration of nutrients in the cells. The ratios between carbon, nitrate and phosphate are kept constant to the values proposed by Takahashi et al. (1985) in all living and non-living pools of organic matter. However, internal concentrations of iron in both phytoplankton and of silicon in diatoms are prognostically simulated. They depend on the external concentration of these nutrients, on the potential limitation by the other nutrients and on light availability.

Phytoplankton chlorophyll concentration is prognostically simulated following Geider et al. (1998). PISCES simulates semi-labile dissolved organic matter, small and big sinking particles, which differ by their sinking speeds (i.e., $3\,m\,d^{-1}$ and 50 to $200\,m\,d^{-1}$, respectively). Only the internal concentrations of iron, silicon and calcite inside the sinking particles are prognostically simulated. In addition to exchange with organic carbon, dissolved inorganic carbon is also altered by the production and dissolution of calcite. Carbon chemistry in seawater is computed from the distribution of dissolved inorganic carbon and alkalinity. Calcite is prognostically simulated following Maier-Reimer (1993) and Moore et al. (2002). Alkalinity includes the contribution of carbonate, bicarbonate, borate and water ions. Oxygen is prognostically simulated using two different oxygen-to-carbon ratios, one accounting when ammonium is converted to or mineralized from organic matter, the other when oxygen is consumed during nitrification. For carbon and oxygen pools, air–sea exchange follows the Wanninkhof (1992) formulation. Importantly, to ensure conservation of nitrogen in the ocean, annual total nitrogen fixation is adjusted to balance losses from denitrification following Lipschultz et al. (1990), Middelburg et al. (1996) and Soetaert et al. (2000). For the other macronutrients, alkalinity and organic carbon, the conservation is ensured by tuning the sedimental loss to the total external input from rivers and dust. Therefore, carbon and nitrogen cycles are decoupled to a certain degree.

The boundary conditions account for nutrient supply from three different sources: atmospheric dust deposition for iron and silicon (Jickells and Spokes, 2001; Moore et al., 2004; Tegen and Fung, 1995), rivers for carbon (Ludwig et al., 1996) and sediment mobilization for sedimentary iron (de Baar and de Jong, 2001; Johnson et al., 1999). In CNRM-ESM1, riverine input of carbon has been revised from Ludwig et al. (1996) in accounting for the interannual variability of runoff estimated with an offline SURFEX simulation over the 1948–2010 period using the global atmospheric forcing from Princeton University (PGF; Sheffield et al., 2006).

In CNRM-ESM1, the marine biophysical feedback is induced by changes in the penetration of downward irradiance in response to marine biota chlorophyll concentration. This feedback mimics the fact that light absorption in the ocean indeed depends on particle concentration and is spectrally selective (Morel, 1988). The implementation of this mechanism is fully described in Lengaigne et al. (2006, 2009) for an ocean forced configuration and Mignot et al. (2013) for a current ocean coupled configuration. It is derived from an accurate 61 spectral band formulation proposed by Morel (1988) using three large wavebands: blue (400–500 nm), green (500–600 nm) and red (600–700 nm). These three bands correspond to the spectral domain of maximum absorption for chlorophyll. The chlorophyll-dependent attenuation coefficients depend on the three-dimensional chlorophyll field predicted by PISCES. They are computed at each time step from a power-law relationship fitting to the coefficients computed from the full spectral model of Morel et al. (1988). This biophysical feedback represents a major evolution from the ocean component used in Voldoire et al. (2013) and Séférian et al. (2013).

3 Experimental setup

3.1 Spin-up strategy

The CMIP5 specification requires each model to reach its equilibrium state before kicking off formal simulations, especially for long-term control experiments. To obtain the initial conditions for CNRM-ESM1 preindustrial steady state at year 1850, we first initialize the various physical and biogeochemical components of the model as described below and perform a 400-year-long spin-up simulation using CNRM-ESM1 with all 1850 external forcings (Taylor et al., 2009).

Initialization of the physical components of CNRM-ESM1 relies on previous model outputs from CNRM-CM5.1. This latter model was first initialized from World Ocean Atlas 2005 observations for salinity and temperature (Antonov et al., 2006; Locarnini et al., 2006) and spun up for 200 years. The 801st year of the centennial-long CMIP5 preindustrial run from CNRM-CM5.1 was employed as initial condition for CNRM-ESM1 preindustrial state.

Marine biogeochemical reservoirs were initialized from fields of a previous preindustrial simulation of CNRM-CM5.1 coupled to PISCES. In this previous simulation, PISCES state variables were initialized from World Ocean Atlas 1993 observations for nitrate, phosphate, silicate and oxygen (Levitus et al., 1993) and the Global Ocean Data Analysis Project (Key et al., 2004) for alkalinity and prein-

dustrial dissolved inorganic carbon (DIC). From this initialization, this intermediate version of the ESM was integrated online for 1100 years.

Land biogeochemical reservoirs were initialized from zero and spun up using an acceleration approach for soil carbon and wood during the first century of the spin-up simulation. This approach consists in updating the wood growth, the litter and soil biogeochemistry modules several times per time step with constant incoming carbon fluxes and physical conditions allowing for the various reservoirs of carbon to fill up much faster. As a result of this approach, soil carbon and wood reservoirs were respectively spun up for 21 800 and 1200 years.

Finally, both physical and carbon cycle components of CNRM-ESM1 benefit from an physical adjustment under 1850 preindustrial control conditions for 400 years. Section 4.1 describes the residual drifts of the model at quasi-equilibrium state.

3.2 CMIP5 preindustrial control and historical simulations

Following CMIP5 specifications (Taylor et al., 2009), CNRM-ESM1 has performed several CMIP5 long-term core experiments and part of the tier-1 experiments.

The preindustrial control simulation, *piControl,* is integrated for 250 years using constant external forcing prescribed at year 1850 conditions and starting from the last year of the online adjustment simulation. That is, atmospheric concentrations of greenhouse gases are set to 284.7 ppmv, 790.9 ppbv and 275.4 ppbv for CO_2, CH_4 and N_2O, respectively. Those of chlorofluorocarbons (CFC-11 and CFC-12) are set to zero. Influence of natural aerosols is prescribed using the optical depths of five types of tropospheric aerosols (black carbon, sea salt, sulfate, dust and particle organic matter) from a previous simulation of the coupled Climate-Chemistry Model (LMDZ-INCA) forced with CMIP5 prescribed emissions (Szopa et al., 2013). Stratospheric volcanic aerosols are prescribed similarly but using a long-term average climatology from a last millennium simulation performed with the NCAR Community Climate System Model (Ammann et al., 2007).

The 20th century experiment, *historical*, is performed from 1850 to 2005. This simulation starts from the CNRM-ESM1 states of the last year of the online adjustment simulation. The modern evolution of the external forcings of both atmospheric greenhouse gases and incoming solar irradiance follows the recommended yearly average observations (Taylor et al., 2009). The monthly temporal and spatial variability of the five tropospheric aerosols also rely on a LMDZ-INCA simulation (Szopa et al., 2013) while those of stratospheric sulfate aerosol concentrations from explosive volcanoes are derived from a 20th century reconstruction of the NCAR Community Climate System Model (Ammann et al., 2007).

Note there is no land-cover change related to anthropogenic land use in the abovementioned simulations. The fraction of vegetal cover is set to the present-day state using the in-house ECOCLIMAP database (Masson et al., 2013a). Therefore, changes in physical and biogeochemical properties of the vegetation due to actual land-cover changes are excluded by design.

4 Results

4.1 Model equilibrium in the preindustrial control simulation

To illustrate the stability of CNRM-ESM1 at the end of the spin-up simulation, we show the global average values of a few variables during the 250 years of the piControl simulation (Fig. 2) and their drifts (Table 1).

In terms of energy balance, the global mean top-of-atmosphere (TOA) net radiative balance is about $3.57 \pm 0.23 \, \mathrm{W \, m^{-2}}$, while the global mean net surface radiation flux (NSF) is $0.87 \pm 0.24 \, \mathrm{W \, m^{-2}}$ (Fig. 2a). The imbalance in the energy budget between the surface and TOA (about $2.7 \, \mathrm{W \, m^{-2}}$) is predominantly due to the non-conservation of energy of the spectral atmospheric model and, to a lesser extent, its coupling with the ocean model. Taking apart this non-conservation offset in TOA net radiation flux, there is no discernible deviation between year-to-year fluctuation between the TOA and NSF net radiation fluxes.

In terms of global-scale climate indices, the global mean surface temperature ($T_{2\,\mathrm{m}}$) and sea surface temperature (SST) over the piControl period are 12.52 ± 0.15 and $17.76 \pm 0.1 \, °C$, respectively (Fig. 2b). They both display almost no drift over the duration of the piControl simulation (Table 1). We use soil wetness index (SWI) and sea surface salinity (SSS) to evaluate the stability of the simulated water cycle (Fig. 2c). These both have almost no drift (Table 1), confirming that the water cycle is closed. Also, there is no drift in both Northern Hemisphere and Southern Hemisphere sea-ice volume (NIV and SIV, respectively) for which long-term means are respectively 20.88 and $6.25 \times 10^3 \, \mathrm{km^3}$ (Fig. 2d).

With regard to the simulated global carbon cycle, Fig. 2e shows that the natural carbon cycle is stable over the piControl simulation with terrestrial and oceanic carbon fluxes of 0.75 ± 0.57 and $-0.94 \pm 0.13 \, \mathrm{Pg \, C \, year^{-1}}$, respectively. Both terrestrial and oceanic components of the simulated carbon cycle exhibit drifts smaller than $10^{-3} \, \mathrm{Pg \, C \, year^{-1}}$ demonstrating that soil and deep ocean carbon stocks have reached a steady state. Deviation from zero in the terrestrial carbon flux is essentially explained by missing perturbations or processes in ISBA such as fire-induced CO_2 emissions or riverine-induced carbon transport from land to oceans (Battin et al., 2009; Regnier et al., 2013). Natural ocean carbon
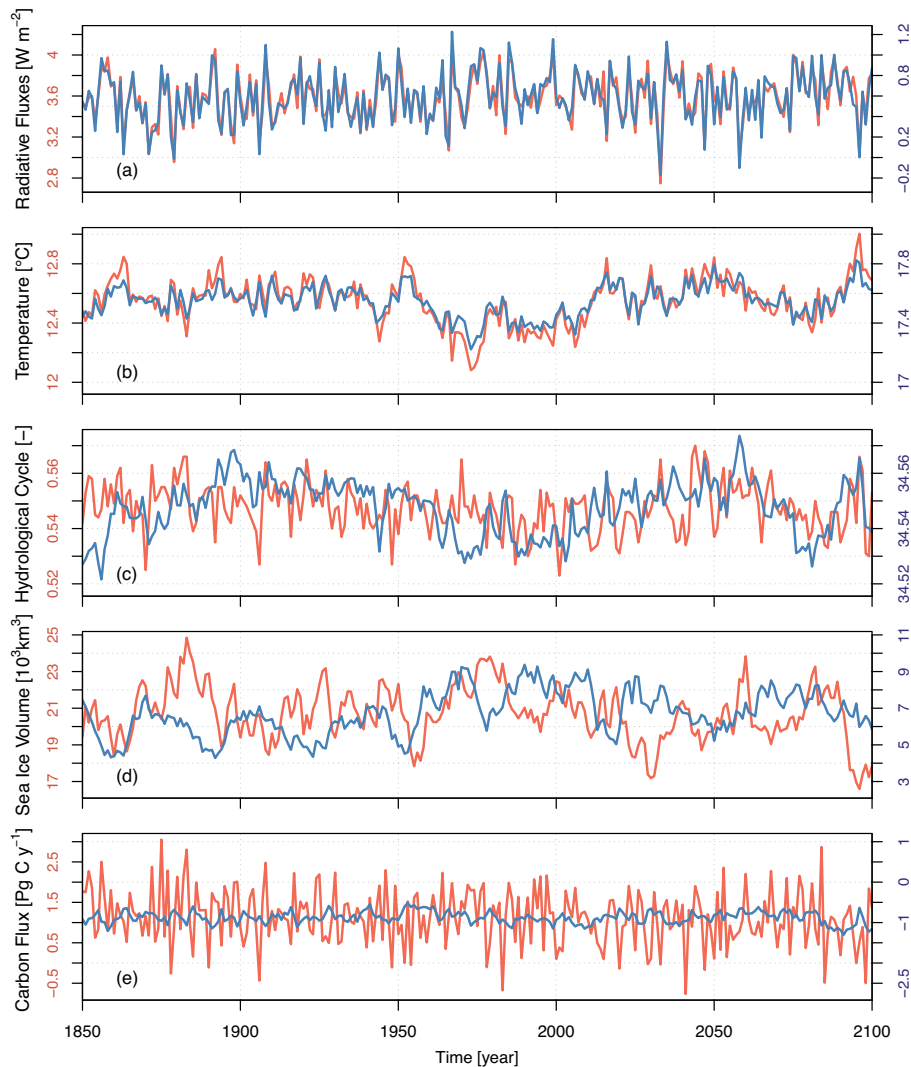
Figure 2. Time series of various climate indices along the 250-year-long control simulation. **(a)** Net radiative fluxes at the top of the atmosphere (in red, left y axis) and surface (in blue, right y axis) are used to assess the stability of the climate energy flow in the model; **(b)** near-surface global average temperature (in red, left y axis) and global-averaged sea surface temperature (in blue, right y axis); **(c)** soil wetness index (in red, left y axis) and sea surface salinity (in blue, right y axis) are used as proxy of the hydrological cycle; **(d)** sea-ice volume in the Northern Hemisphere (in red, left y axis) and in the Southern Hemisphere (in blue, right y axis) are used to evaluate the stability of the cryosphere component in CNRM-ESM1; **(e)** global carbon fluxes over land (in red, left y axis) and over ocean (in blue, right y axis) are used to assess the equilibration of the global carbon stock. For carbon fluxes, positive (negative) fluxes indicate an uptake (outgassing) of CO_2 by land or ocean.

outgassing falls within the upper range of ocean inverse estimates (Jacobson et al., 2007; Mikaloff Fletcher et al., 2007).

4.2 Late 20th century climatology

4.2.1 Land physical drivers

In the following, we focus on the physical drivers of the global carbon cycle. From a land perspective, surface temperature (T_{2m}), precipitation (PR) and photosynthetically active radiation (PAR) are the prominent factors controlling the rate of photosynthetic activity as well as the rate of autotrophic

and heterotrophic respiration, and hence the net land–air exchange of carbon.

Compared to the CRUTV4 data set (Harris et al., 2013) over the period 1986–2005, CNRM-ESM1 displays a global annual-averaged bias of $-3\,°C$ in T_{2m} over continents. In Northern Hemisphere winter (DJFM: December–January–February–March; Fig. 3a) simulated T_{2m} is generally lower than the observations except for some regions (e.g., northeast Siberia, south of Australia and part of Argentina). The mean bias over continents in boreal winter is about $-4\,°C$ and can reach up to $-6\,°C$ over mountain regions. Fig-

Table 1. Drift in climate indices used to evaluate the equilibrium of CNRM-ESM1's physical and biogeochemical components. The drifts are computed over the 250-year-long preindustrial simulation of CNRM-ESM1 for the top of the atmosphere net radiative balance (TOA), the net surface heat flux (NSF), the near-surface temperature ($T_{2\,m}$), the sea surface temperature (SST), the sea surface salinity (SSS), the soil wetness index (SWI), the northern and southern sea-ice volume (NIV and SIV, respectively) as well as the land and ocean global carbon fluxes (LCF and OCF).

	TOA [W m^{-2}]	NSF [W m^{-2}]	$T_{2\,m}$ [°C]	SST [°C]	SWI [–]	SSS [psu]	NIV [10^3 km^3]	SIV [10^3 km^3]	LCF [Pg C year^{-1}]	OCF [Pg C year^{-1}]
Drift [units century^{-1}]	4.4×10^{-4}	4.5×10^{-4}	-1.2×10^{-5}	9.6×10^{-5}	-1.6×10^{-5}	-1.9×10^{-5}	-4.4×10^{-3}	7.2×10^{-3}	-1.5×10^{-4}	-2.0×10^{-4}
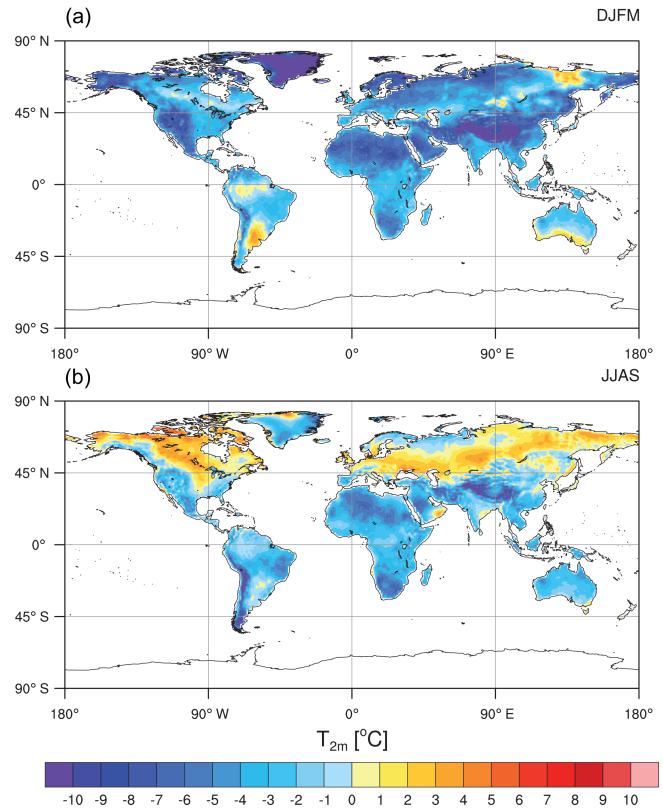
Figure 3. Biases in simulated near-surface temperature ($T_{2\,m}$) compared to the CRUTV4 observations (Harris et al., 2013) averaged 1986–2005. Winter **(a)** and summer **(b)** periods are computed from DJFM and JJAS months.
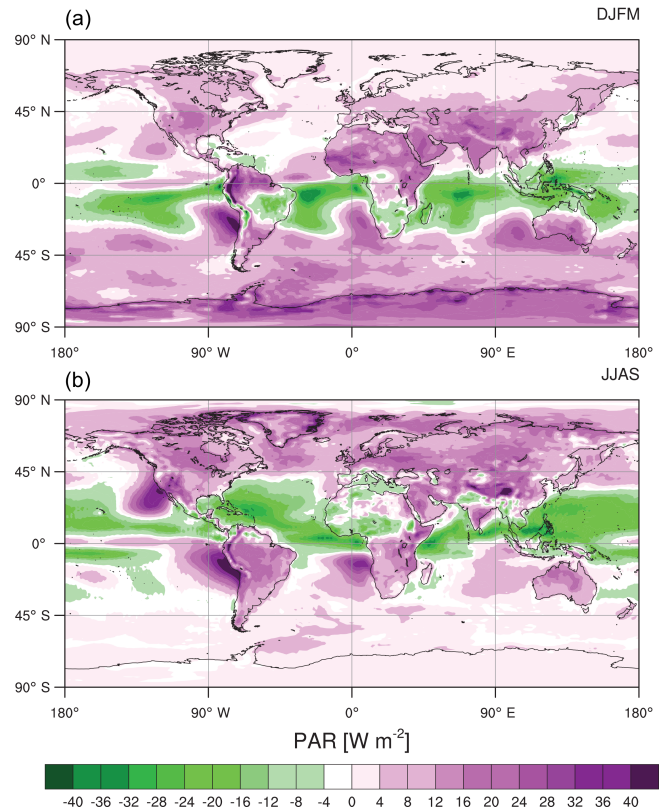
ure 3b shows that simulated summer (i.e., JJAS: June–July–August–September) $T_{2\,m}$ is also generally colder than the observations ($-0.8\,°C$ in global average) over a large fraction of the continents. Only the most northern domains of the Northern Hemisphere display a warm bias that can reach up to $3\,°C$ in the north of Canada. The geographical structure of the $T_{2\,m}$ bias compares well with those detailed in Voldoire et al. (2013). Such an agreement in the bias structure for $T_{2\,m}$ was expected since both models rely on the same physical parameterizations for both the atmosphere and land-surface physics. Small deviations between CNRM-CM5 and CNRM-ESM1 mean state can be essentially attributed to the land carbon cycle, which appears to amplify the global average annual cold bias of $0.8\,°C$ (with seasonal differences between CNRM-ESM1 and CNRM-CM5 of -0.7 and $-1\,°C$ in boreal winter and summer, respectively). This cooling is due to the enhanced evapotranspiration by the interactive terrestrial biosphere compared to the fixed one in CNRM-CM5.

Figure 4 shows the regional structure of the PR bias of CNRM-ESM1 with respect to the Global Precipitation Climatology Project (GPCP) observations (Adler et al., 2003). Over continents, CNRM-ESM1 slightly underestimates the amount of the seasonal PR except over Asia, the western
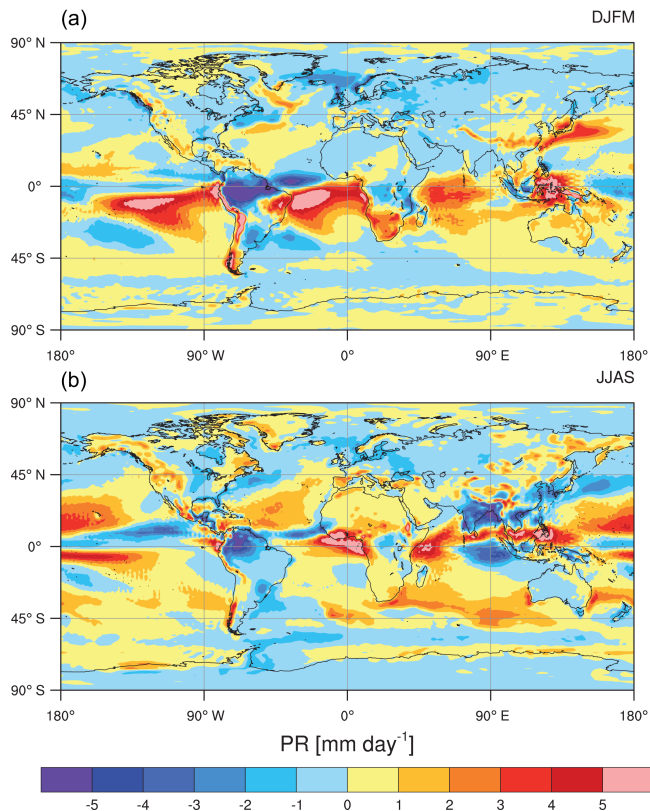
Figure 4. Biases in simulated precipitation (PR) compared to the GPCP observations (Adler et al., 2003) averaged over 1986–2005. Winter **(a)** and summer **(b)** periods are computed from DJFM and JJAS months.


Figure 5. Biases in simulated photosynthetically available radiation (PAR) compared to the Surface Radiation Budget (SRB) satellite-derived observations (Pinker and Laszlo, 1992) averaged over 1986–2005. Winter **(a)** and summer **(b)** periods are computed from DJFM and JJAS months.

coast of America and Australia. The major regional bias in seasonal PR is found over Amazonia, where PR is underestimated by 2 and 5 mm day^{-1} in boreal summer and winter, respectively. Similar to state-of-the-art Earth system models, CNRM-ESM1 displays an excess of precipitation over the oceans. This excess is especially strong in the southern part of the tropical oceans and is associated with the overestimated seasonal latitudinal migration of the Intertropical Convergence Zone (ITCZ). The land biosphere biophysical coupling induces small but noticeable changes in the global hydrological cycle between CNRM-CM5 and CNRM-ESM1. Although weak, changes induced by the ISBA biophysical coupling slightly affect the representation of the seasonal cycle in PR over the vegetated regions (Fig. S1 in the Supplement). These lead to improve the simulated PR in CNRM-ESM1 compared to CNRM-CM5 over some vegetated regions during the growing season (spring–summer). Between 30 and 60° N, the average error in simulated PR compared to GPCP is reduced by 0.12 mm day^{-1} with CNRM-ESM1 compared to that of CNRM-CM5. Over the tropics (30° S–30° N), simulated PR is also improved in CNRM-ESM1 but to a lesser extent with a reduction of the average error by 0.06 mm day^{-1} with respect to GPCP. Although PR have

been improved over some regions, their geographical pattern has been degraded in CNRM-ESM1 compared to CNRM-CM5, especially during the winter.

Compared to Surface Radiation Budget (SRB) satellite-derived observations (Pinker and Laszlo, 1992), CNRM-ESM1 overestimates the PAR globally (Fig. 5). Major biases are found over continents except for some regions in the tropics. The magnitude of the seasonal biases is weaker in Northern Hemisphere winter than in summer when regional biases reach up to 20–30 W m^{-2} over the western border of the continents. Regions where PAR is underestimated match reasonably well with those showing too intense precipitations compared to the GPCP data set (Fig. 4). The general overestimation in PAR is due to the substantial underestimation in low cloud cover in CNRM-ESM1 consistent with CNRM-CM5. Biases in PAR are also found over ocean upwelling system and are linked with an underestimated fraction of stratocumulus.

4.2.2 Ocean physical drivers

From an oceanic perspective, temperature is as important as over land surface because it sets the marine biota's growth
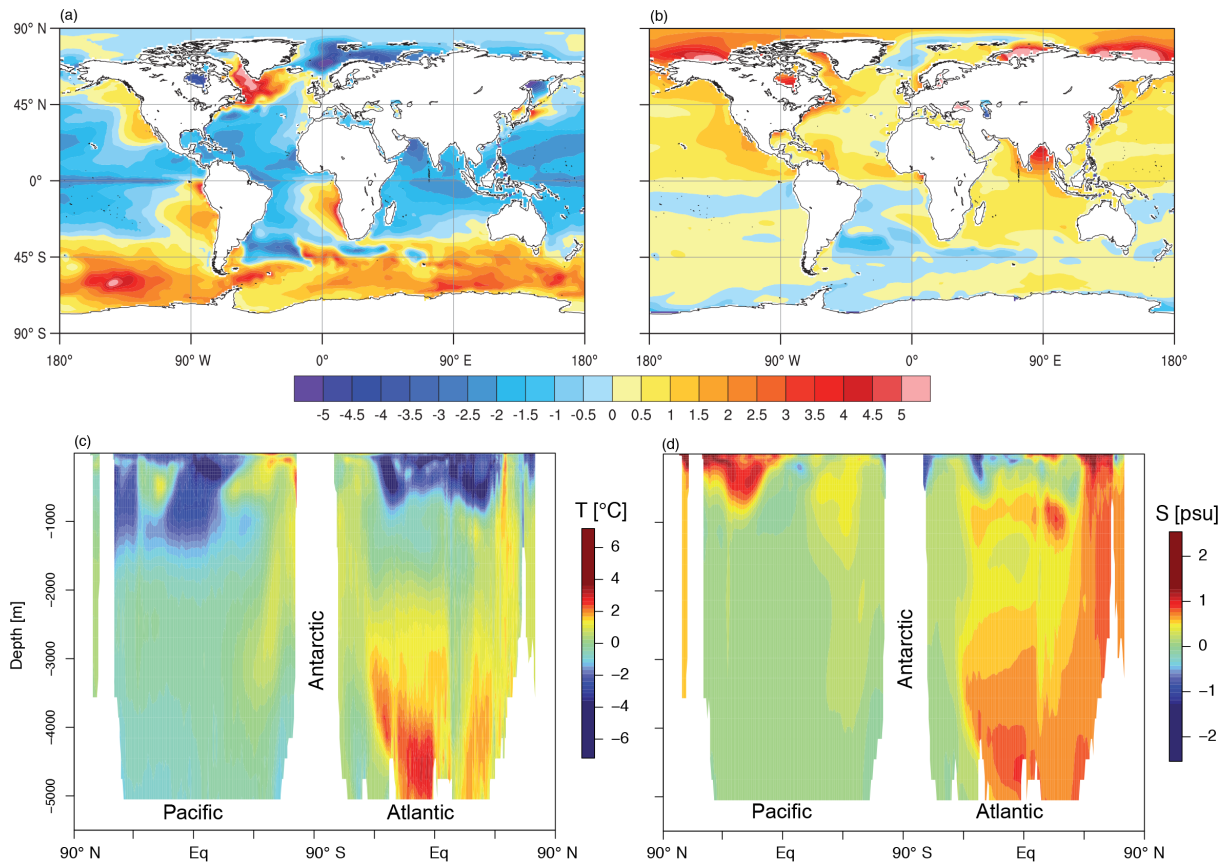
Figure 6. Annual bias patterns of simulated temperature T and salinity S averaged over 1986–2005 compared to the WOA2013 observations (Levitus et al., 2013). Surface biases for sea surface temperature **(a)** and salinity **(b)** are represented using the same color bar. Vertical structure of biases for temperature **(c)** and salinity **(d)** are estimated using zonal-average biases from WOA2013 across the Atlantic and Pacific oceans.

rate, playing a large role in the biological-mediated processes (e.g., export, soft tissue pump). In addition, both temperature (T) and salinity (S) control the solubility of CO_2 into seawater and the chemical-mediated air–sea exchanges of carbon. The mixed-layer depth (MLD) and the sea-ice cover (SIC) are also critical drivers of the ocean carbon cycle as they both contribute to the nutrient-to-light limitation in the high-latitude oceans (Sarmiento and Gruber, 2006). In the following, we assess the representation of these drivers.

Compared to WOA2013 data products (Levitus et al., 2013), CNRM-ESM1 realistically simulates both the mean annual sea surface temperature and sea surface salinity, both in terms of amplitude and spatial distribution, as shown in Fig. 6a and b. Moderate positive biases in sea surface temperature and sea surface salinity are found in the Southern Ocean and in the eastern boundary upwelling systems. Strong biases in sea surface salinity are found in the Labrador and Arctic seas. While most of these biases are related to an overestimated atmospheric surface heating, biases in the Labrador Sea and in the Arctic are essentially due to erroneous rep-

resentation of the mixed-layer depth and the Arctic sea-ice cover. These points will be further detailed below.

At depth, the vertical structures in simulated T and S display biases from those estimated from WOA2013 observations. T is underestimated by $\sim 2\,°C$ within the first 1000 m of the Atlantic and Pacific oceans, except in the deep water formation zone (North Atlantic, North Pacific and Southern Ocean), where the model displays positive biases. The largest deviation in vertical structure of simulated S from that estimated from WOA2013 are found in deep water formation zones where haline biases of about $\sim 1\,psu$ tend to compensate for the warm bias in T, enabling deep convection of water masses. Because of this compensating mechanism, the flow of North Atlantic deep waters (NADW) fueling the Atlantic meridional overturning circulation is about $26.1 \pm 2\,Sv$ at $26.5°\,N$ in CNRM-ESM1 averaged over the 1850–2005 period. This value is stronger than the observations-derived estimate of $18 \pm 5\,Sv$ (Talley et al., 2003) or the observations from RAPID-MOCHA monitoring array over 2004–2007, estimating the flow at about $18.5 \pm 4.9\,Sv$ (Johns et al., 2011). In the Southern Ocean, the flow of Antarctic bot-
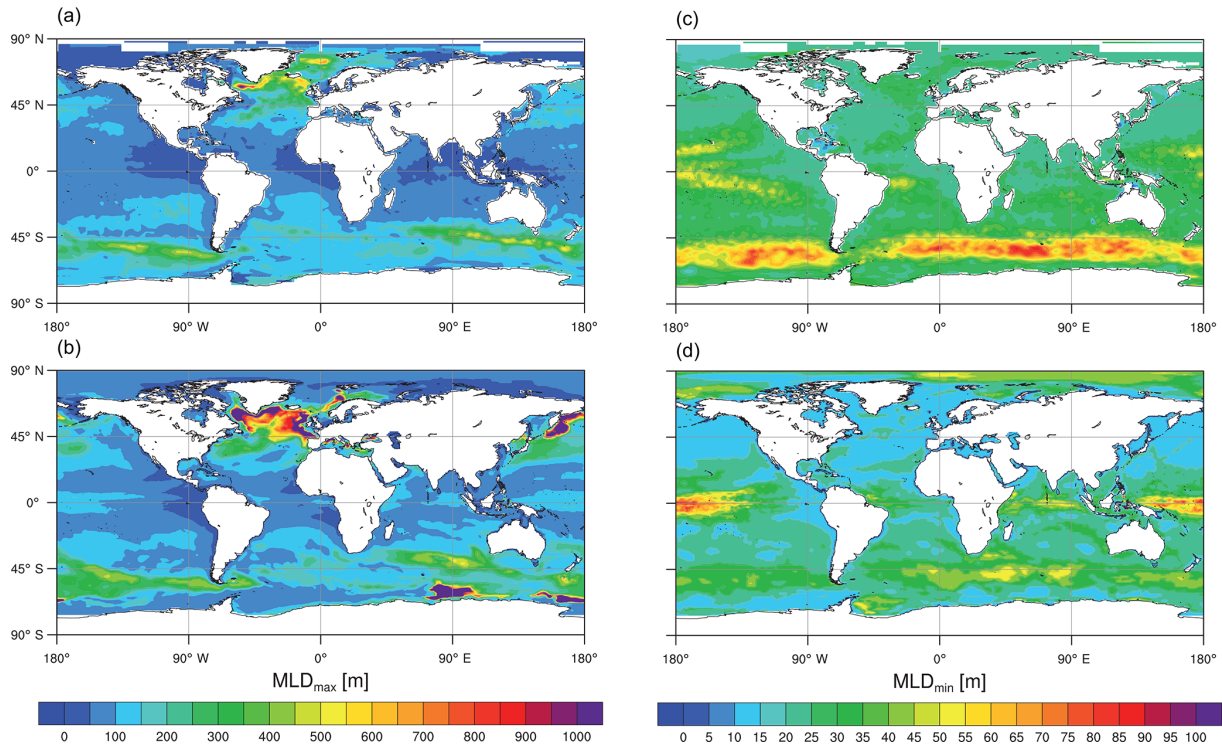
Figure 7. Composite of yearly extremum of mixed-layer depth over 1986–2005. Left panels represent the maximum mixed-layer depth (MLD$_{max}$) for **(a)** observations (Sallée et al., 2010) and **(b)** CNRM-ESM1. Right panels represent the minimum mixed-layer depth (MLD$_{min}$) for observations **(c)** and CNRM-ESM1 **(d)**.

tom water (AABW) is about $11.6 \pm 1\,\text{Sv}$ in CNRM-ESM1 averaged over the 1850–2005 period. This flow of AABW is in agreement with the deep flow of waters compared to the observed estimate of $10 \pm 2\,\text{Sv}$ (Orsi et al., 1999). Consequently, the flow of deep water masses in CNRM-ESM1 has been improved with regards to that of CNRM-CM5, which ranges between 3.4 and 6.2 Sv over the same period (Séférian et al., 2013; Voldoire et al., 2013). As detailed in several intercomparison studies (de Lavergne et al., 2014; Heuzé et al., 2013; Sallée et al., 2013; Séférian et al., 2013), CNRM-CM5 substantially underestimated the flow of AABW leading to an erroneous distribution of hydrodynamical and biogeochemical fields at depth. Here, although stronger than the observation-based estimates, the flow of NADW and AABW improves the deep ocean ventilation as well as the distribution of tracers at depth (Sect. 4.2.5).

As mentioned above, an accurate representation of spatial and temporal MLD is essential for numerous ocean biogeochemical processes. For example, winter mixing entrains carbon- and nutrient-rich deep waters to the surface, which play an important role in the transfer of CO_2 across the sea-to-air interface. In summer, MLD contributes to the nutrient-to-light limitation of the phytoplankton growth in high-latitude oceans. The maximum and minimum mixed-layer depth (hereafter, MLD$_{max}$ and MLD$_{min}$) are respectively used as a proxy of the winter and summer MLD since

mixing occurs randomly during seasons in response to numerous environmental factors (wind, stratification, local instability, etc.) that present a large spatiotemporal variability. Figure 7 presents composites of yearly MLD$_{max}$ and MLD$_{min}$ as simulated by CNRM-ESM1 in averaged over the 1986–2005 period and derived from observations (Sallée et al., 2010). Figure 7a and b show that CNRM-ESM1 reproduces the main regional pattern of MLD$_{max}$ compared to the observation-derived estimates. However, the model tends to simulate too large and too deep mixing sites in the North Atlantic, the North Pacific and the Southern Ocean. In the North Atlantic, the larger than observed mixed volume of surface dense waters (combination of surface area and depth of the mixing zone) is at the origin of the strong flow of NADW simulated in CNRM-ESM1. In the Southern Ocean, although open-ocean polynyas were observed from space in the past decades (Cavalieri et al., 1996; Comiso, 1999), their locations are erroneous in CNRM-ESM1 similarly to several other CMIP5 Earth system models (de Lavergne et al., 2014). CNRM-ESM1 simulates open-ocean polynyas in the Indian basin and close to the Ross Sea but not in the Atlantic basin as observed from space between 1974 and 1976.

Compared to the observation-derived estimates, CNRM-ESM1 captures the main regional pattern of MLD$_{min}$ but the model fails at reproducing the deepest values of mixing in the Southern Ocean and the tropics. This bias might be linked to
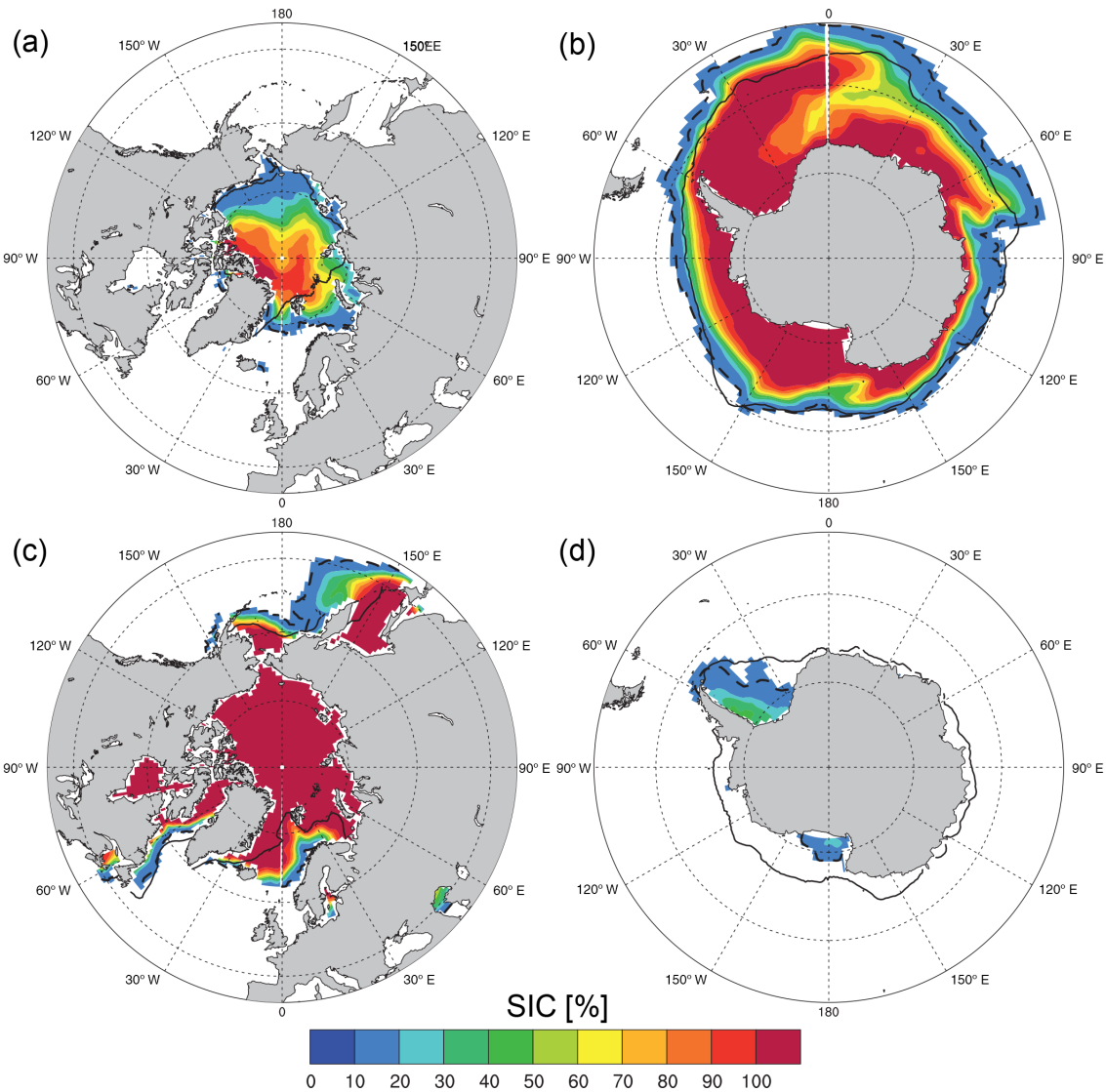
Figure 8. Sea-ice cover (SIC) as simulated by CNRM-ESM1 averaged over 1986–2005. Top panels represent composite of September sea-ice cover, while bottom panels are for March. Iso-15 % of SIC serves as comparison between model results and NSIDC observations (Cavalieri et al., 1996) averaged over 1986–2005; model results and observations are indicated with dashed and solid black lines, respectively.

the current parameterization of the ocean mixing employed in CNRM-ESM1 because previous model versions using this parameterization also exhibited similar patterns of errors as detailed in Séférian et al. (2013) and Voldoire et al. (2013).

Similarly to the MLD, SIC is an important driver of the ocean carbon cycle. It constitutes a physical barrier for exchange of CO_2 between the ocean and the atmosphere leading to an accumulation of carbon-rich waters below the sea ice (Takahashi, 2009). It also plays a large role in the seasonal timing of algal blooms (Wassmann et al., 2010). Compared to the MLD, seasonal variations of sea ice are strongly and directly responsive to the seasonal fluctuations of atmospheric forcing. Therefore, it matters that the model is able to accurately capture the spatial distribution and timing of annual

minimal and maximal sea ice covers in both Hemispheres. For this purpose, we evaluate differences between composites of simulated and observed SIC (Cavalieri et al., 1996) for September and March over the 1986–2005 period (Fig. 8). In the Arctic Ocean, CNRM-ESM1 underestimates SIC in the Beaufort, Chukchi and eastern Siberian seas in September, while too much sea ice tends to be present in the Barents Sea (Fig. 8a). In March, SIC is largely overestimated in the Barents and Nordic seas, as well as in the Bering and Okhotsk seas on the Pacific Ocean side, showing that the simulated winter sea-ice edge spreads too far south and east in these regions (represented with iso-15 % in Fig. 8c). On the contrary, SIC is slightly underestimated in the Labrador Sea and Baffin Bay in March (Fig. 8c). This too far north ice edge comes
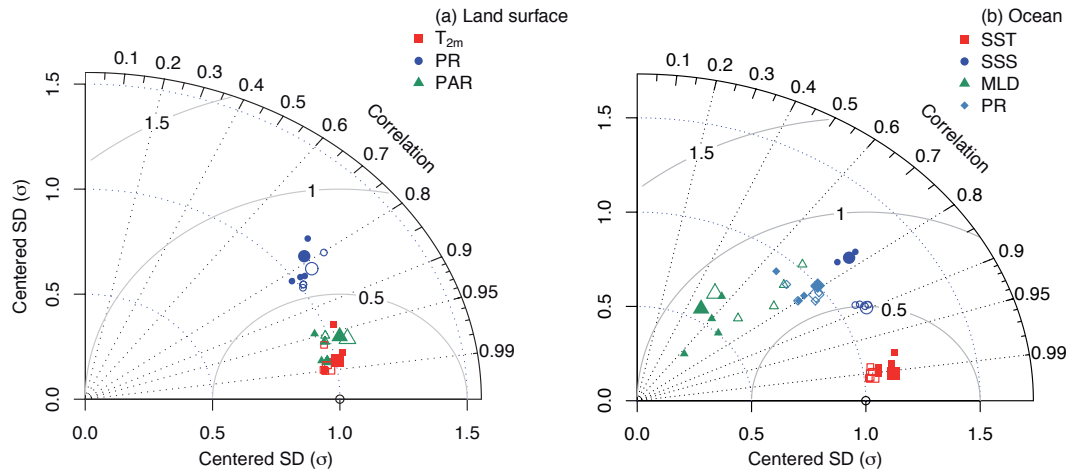
Figure 9. Taylor diagrams showing the correspondence between model results and observations for CNRM-ESM1 and CNRM-CM5.2. Near-surface temperature ($T_{2\,m}$), precipitation (PR) and photosynthetically available radiation (PAR) are used to assess model performance over land surface. Sea surface temperature (SST), sea surface salinity (SSS), mixed-layer depth (MLD) and precipitation (PR) are used to assess model performance over ocean. Filled and empty symbols indicate skills for CNRM-ESM1 and CNRM-CM5.2, respectively. The size of the symbols indicates whether statistics were computed from annual mean climatology or seasonal average (JFM, AMJ, JAS, OND) over 1986–2005.

along with positive SST biases in this region (Fig. 6a), and explains why the simulated deep convection zone is too large and shifted northward in CNRM-ESM1 as shown in Fig. 7.

In the Antarctic Ocean, Fig. 8b shows that the spatial structures of SIC biases mirror somehow the model–data mismatch in MLD as shown in Fig. 7b. That is, in austral winter, CNRM-ESM1 underestimates SIC where erroneous open-ocean deep convection zones are located, namely, offshore Wilkes Land in the Indian Ocean sector (Fig. 8b). Conversely, too much sea ice is simulated in the Atlantic Ocean sector. As in CNRM-CM5.1, simulated summer Antarctic SIC is strongly underestimated, with very little sea ice surviving summer melt in the Weddell and Ross seas (Fig. 8d).

4.2.3 Comparison with previous model version

In the following, we compare the skill of CNRM-ESM1 to the closest version of CNRM-CM5 climate model, called CNRM-CM5.2. Figure 9 summarizes skill-assessment metrics for CNRM-ESM1 and CNRM-CM5.2 in terms of major physical drivers of the global carbon cycle (field maps and patterns of errors are presented in Figs. S2 to S7).

The Taylor diagram for land-surface physical drivers clearly demonstrates that CNRM-ESM1 and CNRM-CM5 display comparable skills except for PR (Fig. 9a). Most of the differences in skills are indeed not significant at a 95 % confidence level; models differ solely in terms of PR for which CNRM-ESM1 produces slightly weaker correlation coefficients.

Over the ocean, Fig. 9b shows further differences between both models. The weakest difference in skill concerns SST for which both models display good agreement with

WOA2013. With regard to the MLD, CNRM-ESM1 displays a slightly better agreement than CNRM-CM5.2 with observation-derived MLD (Sallée et al., 2010) in terms of correlation but strongly underestimates the spatial variations of this field. Major differences are noticeable for SSS. CNRM-ESM1's skill is clearly lower than that of CNRM-CM5.2. To investigate this difference, we have computed the skill of PR over the ocean, since CNRM-CM5.2 contributes to the spatiotemporal distribution of the SSS concomitantly to the runoff and the sea-ice seasonal cycle. Skill in PR over the ocean is similar for both models (blue diamonds on Fig. 9b). A similar finding is noticed for simulated runoff (not shown). Therefore, the difference in simulated SSS between the two models can be attributed to the revised water conservation interface and erroneous distribution of sea-ice cover. In addition, changes in coupling frequency (i.e., 24 to 6 h) might be at the origin of differences in skills between the two models since it impacts sea-ice cover (Fig. 10).

From the small differences in skill between the two models, we can assume that the inclusion of the global carbon cycle and the biophysical coupling have not noticeably altered the simulated mean-state climate in CNRM-ESM1 compared to that of CNRM-CM5.2.

4.2.4 Terrestrial carbon cycle

Now that the physical drivers of the global carbon cycle have been evaluated, we assess the ability of CNRM-ESM1 to replicate available modern observations of the terrestrial carbon cycle. We focus on gross primary productivity (GPP), vegetation autotrophic respiration (Ra) and soil organic carbon content (cSoil) that control the net natural fluxes of
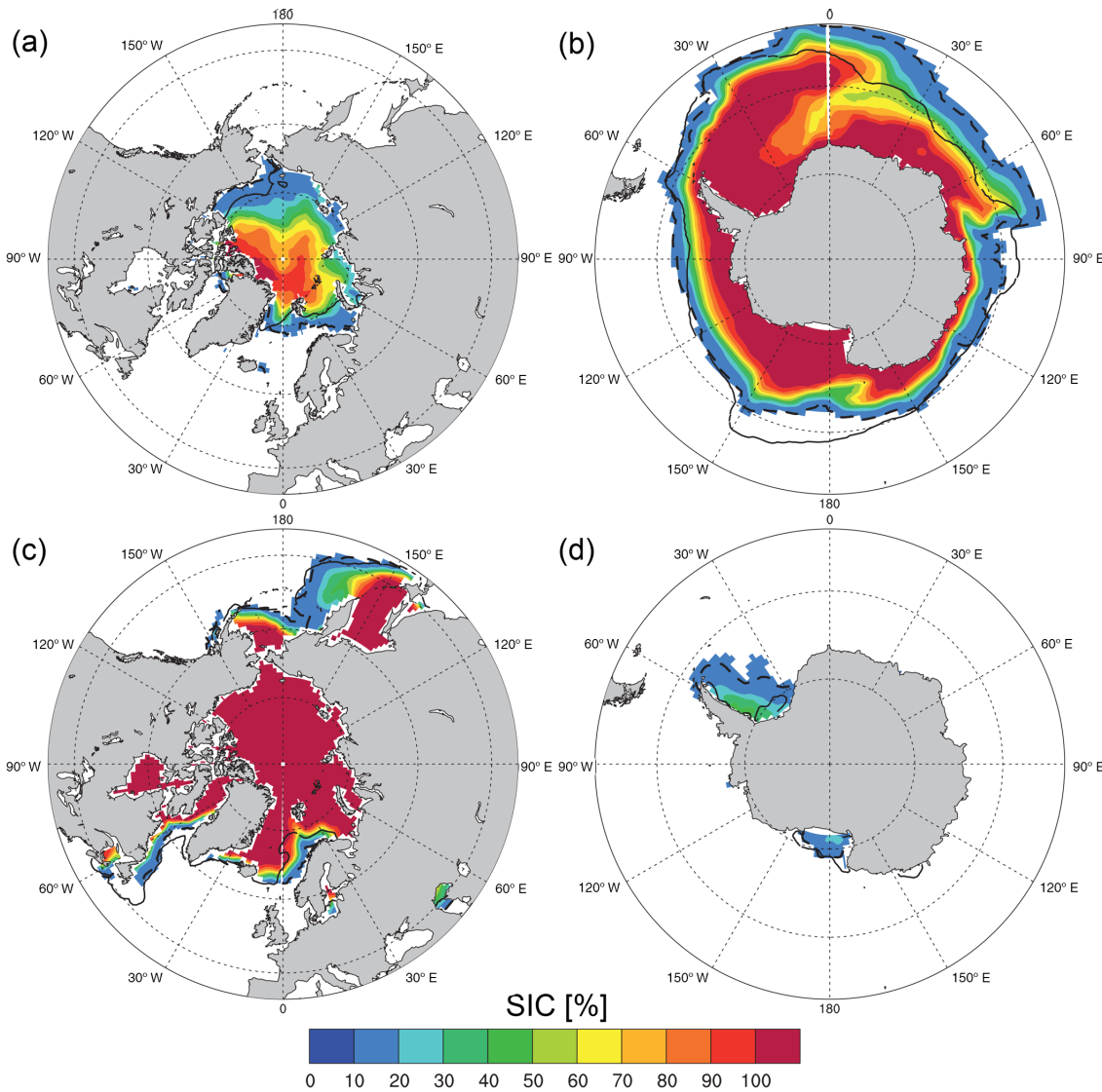
Figure 10. Impact of coupling frequency on sea-ice cover (SIC) as simulated by CNRM-ESM1 averaged over 1986–2005. Top panels represent composite of September sea-ice cover, while bottom panels are for March. Iso-15 % of SIC serves as comparison between model results using a 6 h coupling frequency (dashed lines) and those using a 24 h coupling frequency (solid lines).

CO_2 on land. Simulated budget of vegetation biomass and total ecosystem respiration (TER; sum of autotrophic and heterotrophic respirations) are evaluated against available published estimates. While we can assess the capability of CNRM-ESM1 to fix and emit carbon on land, it is important to note that the CO_2 fluxes due to land use changes are not taken into account in this analysis.

To evaluate CNRM-ESM1 GPP, we rely on two streams of data, namely, the FluxNet-Multi-Tree Ensemble (FluxNet-MTE, Jung et al., 2011) and the MOD17 satellite-derived observations (Running et al., 2004). Figure 11 shows that the annual mean GPP as simulated by CNRM-ESM1 is slightly too strong compared to the observed estimates. The largest model–data mismatch is found in the tropics between 10° N

and 20° S, where CNRM-ESM1 simulates erroneous patterns of high GPP. Over Amazonia, CNRM-ESM1 fails to reproduce the zonal gradient of GPP. Regions of high GPP are in association with overestimated PAR and, to a lesser extent, underestimated PR in summer (Figs. 4 and 5, respectively; see also Fig. S8). The geographical structure of simulated GPP fits the observed over the African and Asian rain forest but its amplitude is overestimated by about $3 \, \mathrm{gC \, m^{-2} \, day^{-1}}$. This regional overestimation impacts both the zonal and global GPP budget, which are larger than the published estimates except > 60° N (Table 2). This stronger-than-observed GPP constitutes a systematic bias of the current version of ISBA. In an offline simulation, Carrer et al. (2013b) showed that ISBA forced with PGF overestimates global GPP by
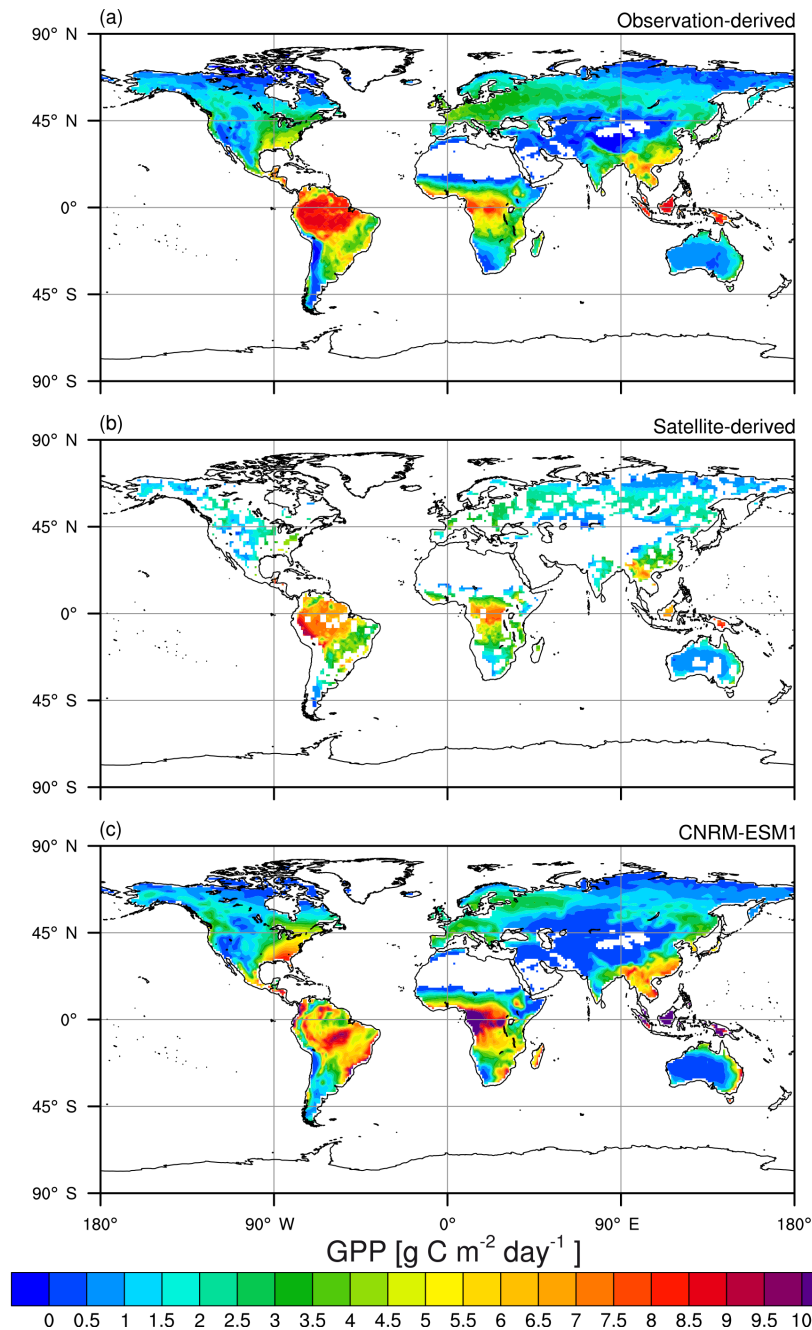
Figure 11. Annual-mean terrestrial gross primary production (GPP). Values are given for **(a)** observation-derived FluxNet-MTE (Jung et al., 2011) averaged over 1986–2005, **(b)** satellite-derived observation from MODIS over 2000–2013 and **(c)** CNRM-ESM1 over 1986–2005.

$60 \, \mathrm{Pg} \, \mathrm{C} \, \mathrm{year}^{-1}$. Regional biases in GPP are partly compensated by overestimated Ra (Fig. 12). Simulated Ra agrees reasonably well with satellite-derived estimates except in the tropics. This bias compensation between GPP and Ra is analyzed in detail by Joetzjer et al. (2015). In this study, the authors demonstrate that the current parameterizations of Ra and water stress in ISBA are not adequate for tropical broadleaf trees (Fig. 1). Considering that these results were

deduced from offline simulations forced with in situ observations, we can assume here that biases in GPP and Ra result from a combination of erroneous ecophysiological parameterizations and biases in physical drivers in CNRM-ESM1.

Despite these biases, the global partitioning between vegetation biomass and soil carbon is realistic with 596.7 and 2105 Pg C compared to the observed estimates of 560 ± 94 (DeFries et al., 1999) and 1750 ± 250 Pg C (Houghton,

Table 2. Regional and global budget of gross primary production (GPP) and terrestrial ecosystem respiration (TER) as simulated by the CNRM-ESM1 and estimated from the FluxNet-MTE data product. Values in brackets indicate the ratio between the autotrophic respiration (Ra) and TER. The uncertainties for the FluxNet-MTE data product derive from the regional partitioning of global mean uncertainties published in Jung et al. (2011). GPP and TER fluxes are determined from a yearly average over 1986–2005.

Regions	CNRM-ESM1	MTE-FluxNet	CNRM-ESM1	MTE-FluxNet
	GPP [Pg C year^{-1}]		TER [Pg C year^{-1}]	
High-latitude north (> 60° N)	2.6	4.8 ± 0.8	2.5 (38 %)	3.1 ± 0.8
Mid-latitude north (20–60° N)	37.9	34.8 ± 2.7	36.23 (52 %)	29.9 ± 2.7
Tropics (20° S–20° N)	73.2	62.3 ± 1.9	72.58 (72 %)	54.8 ± 1.9
Mid-latitude south (20–60° S)	16.1	9.3 ± 0.6	15.6 (56 %)	8.5 ± 0.6
Global	130.0	111.3 ± 6.0	126.9 (64 %)	96.4 ± 6.0
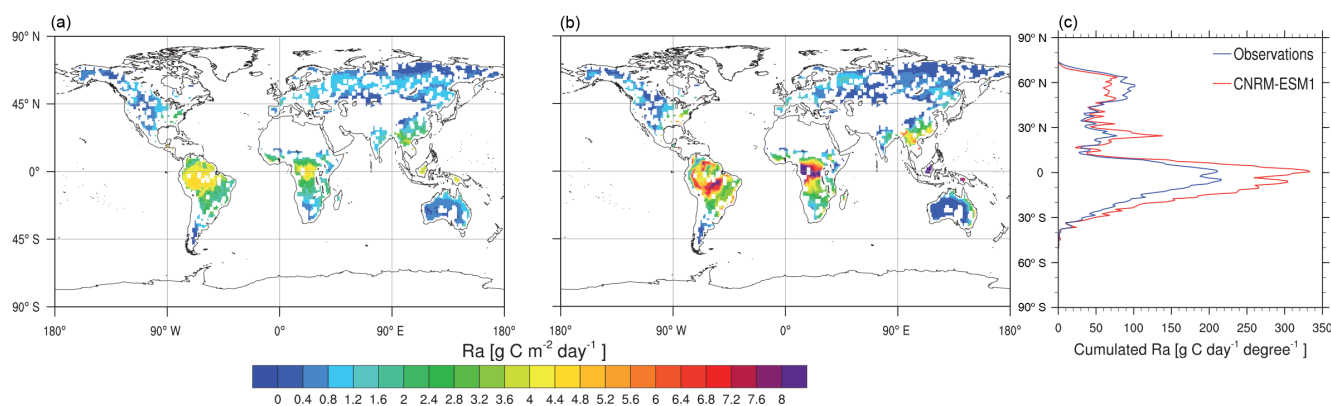
Figure 12. Annual-mean autotrophic respiration (Ra) as estimated from MODIS over 2000–2013 **(a)** and as simulated by CNRM-ESM1 **(b)** over 1986–2005. Panel **(c)** represents the zonal-cumulated Ra in function of latitude for both satellite-derived estimates (in blue) and CNRM-ESM1 (in red).

2007), respectively. Furthermore, the geographical structure of cSoil agrees well with Harmonized World Soil Database (JRC, 2012) except in the Northern Hemisphere (Fig. 13). Although several processes are missing in ISBA to accurately simulate high-latitude carbon stock (e.g., permafrost dynamics, bacterial degradation of the litter, fire-induced turnover), a part of cSoil underestimation can be attributed to the summer warm bias in near-surface temperature (Fig. 3b). This latter tends to enhance heterotrophic respiration of the soil, reducing the soil organic matter ($R > 0.6$, Fig. S2).

Table 2 shows that CNRM-ESM1 overestimates globally terrestrial ecosystem respiration (TER) when compared to the up-scaled measurements of FluxNet-MTE. In the tropics, simulated TER fluxes are 32 % higher than the FluxNet-MTE estimates. As mentioned above, this bias is essentially due to an unrealistic Ra, which amounts to 72 % of TER over the sector in the model. Table 2 shows that the simulated TER is 126.9 Pg C year^{-1}, larger than estimates published by Jung et al. (2011) of $96.4 ± 6.0$ Pg C year^{-1}. Nevertheless, the simulated net land carbon sink (LCS), which can be estimated by subtracting TER from GPP, is 2.19 Pg C year^{-1} in average over the 1986–2005 period and remains within the range

of values estimated from various observation-based methods (IPCC, 2007, 2013; Le Quéré et al., 2014).

4.2.5 Ocean carbon cycle

Compared to the terrestrial carbon cycle, the ocean carbon cycle has already been implemented in previous versions of CNRM-CM5 (Séférian et al., 2013). The modeled marine biogeochemistry components have already benefited from detailed evaluation against modern observations (Frölicher et al., 2014; Séférian et al., 2013), analyses of future projections (Laufkötter et al., 2015) and sensitivity benchmarking (Schwinger et al., 2014). The major difference between CNRM-ESM1 and previous versions of CNRM-CM5 including a marine biogeochemistry module lies in the representation of ocean tracers in the deep ocean. Figure 14 shows that the representation of oxygen, phosphate, nitrate and silicate fields was improved in CNRM-ESM1 at depth, except around 1000 m where the strong flow of NADW tends to alter the distribution of tracers. Below 1500 m, the tracer distribution is in reasonable agreement with the observations with correlation coefficients ~ 0.8. This represents a noticeable improvement with respect to the CNRM-CM5 oxygen
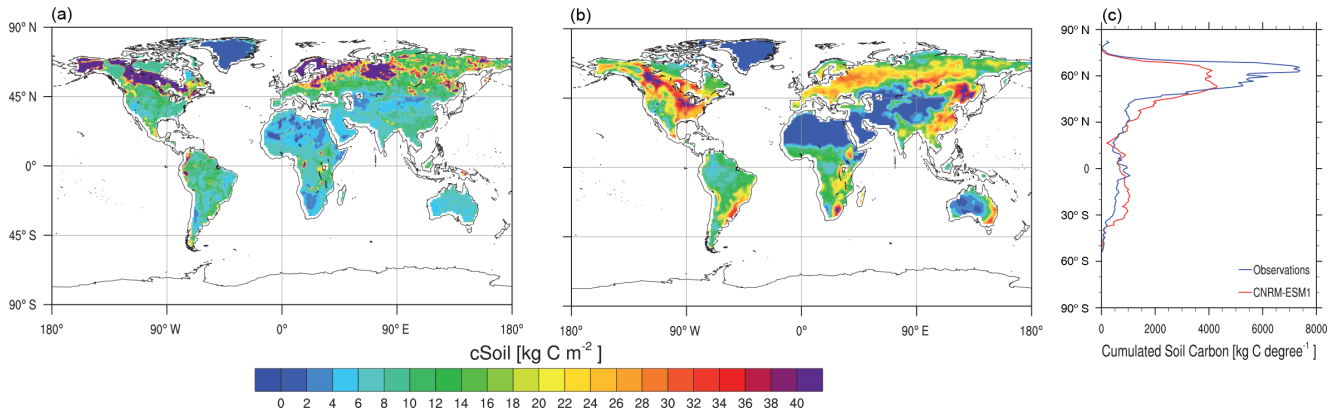
Figure 13. Stocks of modern soil organic carbon (cSoil) as estimated from the FAO/IIASA/ISRIC/ISSCAS/JRC (2012) Harmonized World Soil Database **(a)** and as simulated by CNRM-ESM1 **(b)** averaged over 1986–2005. Panel **(c)** represents the zonally cumulated soil organic stock in function of latitude for both observation-based estimates (in blue) and CNRM-ESM1 (in red).
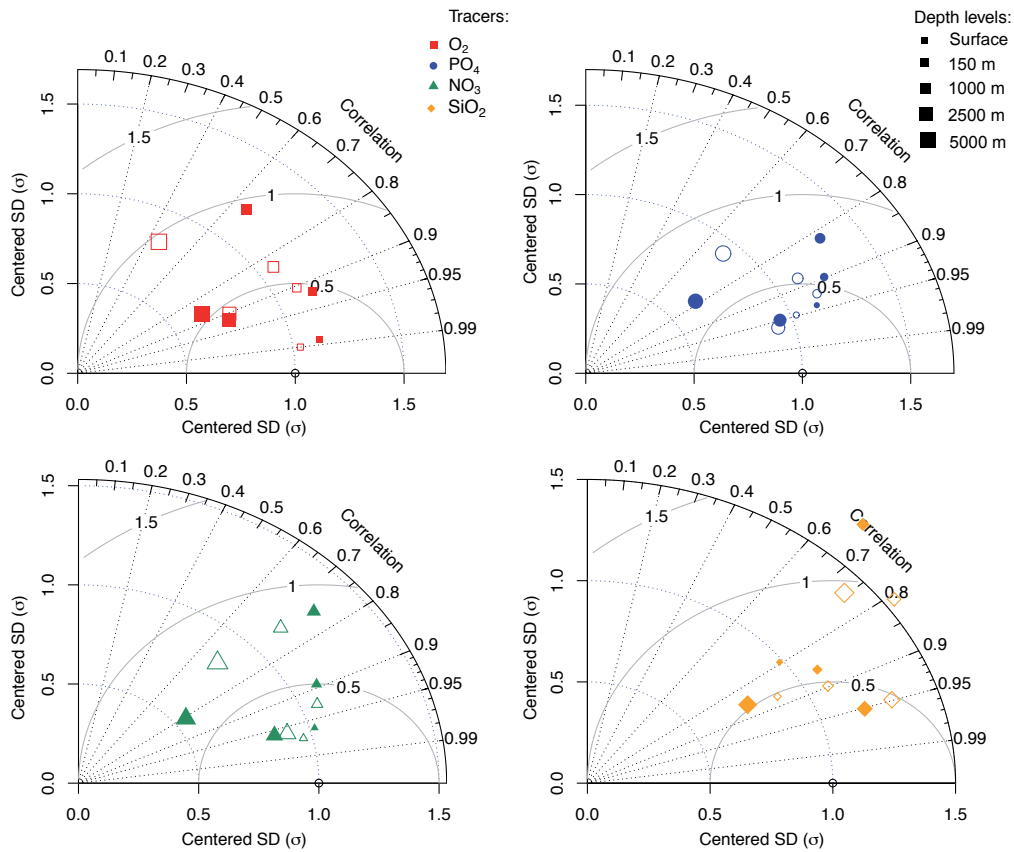

Figure 14. Taylor diagrams showing the correspondence between model results and observations for CNRM-ESM1 and CNRM-CM5.2 (Séférian et al., 2013). Climatological distribution over 1986–2005 of simulated oxygen (O_2), phosphate (PO_4), nitrate (NO_3) and silicate (SiO_2) concentrations are assessed against WOA2013 data product. Filled and empty symbols indicate skills for CNRM-ESM1 and CNRM-CM5, respectively. The size of the symbols indicates the depth at which statistics have been computed.

distribution ($R \sim 0.4$). In addition to nutrients, the vertical distribution of carbon-related fields like dissolved inorganic carbon has been substantially improved in CNRM-ESM1 compared to CNRM-CM5 (Fig. S9), showing a much better agreement with Global Data Analysis Project (GLODAP) observations (Key et al., 2004; Sabine et al., 2004).

In terms of carbon cycling into the ocean, Fig. 15 shows the simulated mean annual sea–air CO_2 fluxes from 1986
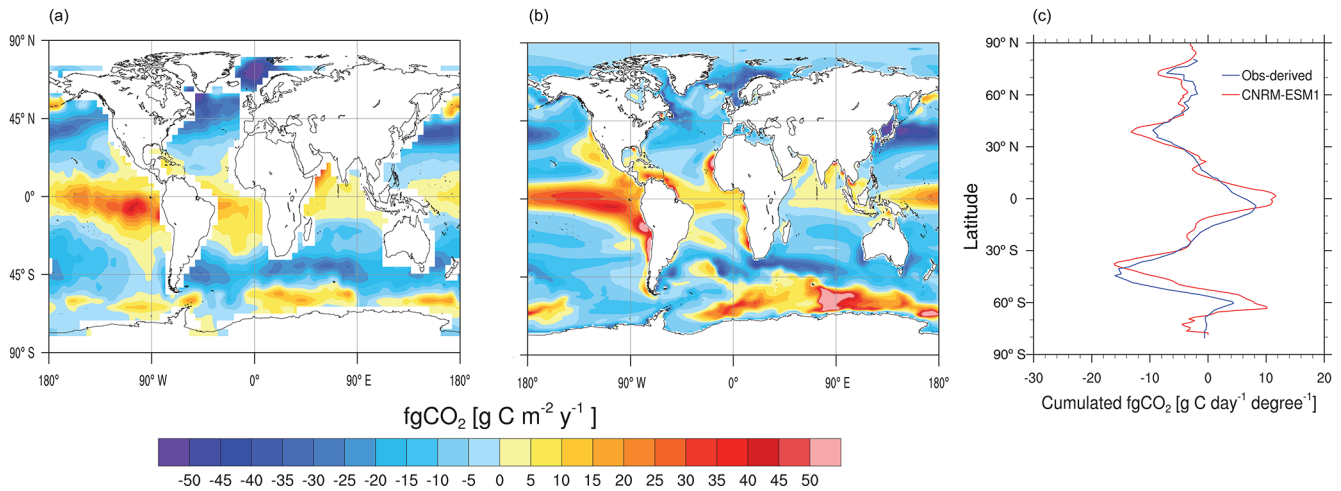
Figure 15. Annual-mean ocean carbon fluxes ($fgCO_2$) as estimated by the Takahashi et al. (2010) database **(a)** and as simulated by CNRM-ESM1 averaged over 1986–2005 **(b)**. Panel **(c)** represents the zonal-cumulated carbon fluxes in function of latitude for both observation-based estimates (in blue) and CNRM-ESM1 (in red). Negative (positive) fluxes indicate an uptake (outgassing) of CO_2.

to 2005 together with observation-based estimates by Takahashi et al. (2010) using 2000 as a single reference year. While the model broadly agrees with the observations in terms of spatial variation for regions of carbon sink (i.e., North Atlantic, North Pacific and between 50 and 40° S), it displays a too strong source of carbon to the atmosphere in the equatorial Pacific and in the Southern Ocean. In the equatorial Pacific, the model–data mismatch is likely related to the decision of Takahashi et al. (2010) to exclude observations from El Niño years from their analysis. Since surface ocean pCO_2 of the eastern tropical Pacific during El Niño events tends to be lower than the long-term mean, the Lamont–Doherty Earth Observatory (LDEO) climatology tends to underestimate outgassing of CO_2 in the equatorial Pacific over the 1986–2005 period. This hypothesis is validated when comparing model results against recent data products derived from statistical Monte Carlo Markov chain or neural network gap-filling methods (Landschützer et al., 2014; Majkut et al., 2014, Fig. S10). In the Southern Ocean, the model–data mismatch is especially pronounced south of 60° S. This bias in $fgCO_2$ is associated with overestimated mixing (Fig. 7), which tends to bring too much deep carbon-rich water masses to the surface, enhancing the outgassing of CO_2. CNRM-ESM1 results display similar discrepancies when compared to other recent observation-derived data products, which coincide with regard to a moderate CO_2 outgassing south of 60° S (Fig. S10). That said, simulated patterns of sea-to-air carbon fluxes in this domain qualitatively agree with the data, showing a combination of source and sink regions.

The storage of anthropogenic CO_2 by the oceans (CO_2^{ANTH}, Fig. 16) provides a complementary view of the ocean carbon fluxes by revealing the chronology of the ocean CO_2 uptake from preindustrial to modern state. Here, we

have chosen to stick to the available observation-derived estimates (GLODAP), which use year 1994 as a single reference year (Key et al., 2004; Sabine et al., 2004). In order to account for the interannual variability of the simulated fields, we chose to analyze yearly average results from CNRM-ESM1 over 1990–2005 (Fig. 16). Furthermore, computation of CO_2^{ANTH} is not straightforward since natural and anthropogenic pools of carbon are not treated separately in PISCES. We approximate consequently CO_2^{ANTH} from the difference between modern and preindustrial stocks of dissolved inorganic carbon. Negative values were set to zero in the computation since they are essentially generated from differences in simulated interannual variability. Ideally, this computation would have required a historical simulation with constant preindustrial atmospheric CO_2 for the sea-to-air CO_2 fluxes. Figure 16 shows that the maximum CO_2^{ANTH} is concentrated in the North Atlantic region. This feature is linked to the large-scale circulation in the surface layer of the ocean, which converges in the North Atlantic, before being exported to depth with the flow of NADW (Pérez et al., 2013). The Southern Ocean also stores a large fraction of CO_2^{ANTH} in association with the subduction of modal and intermediate water masses (Sallée et al., 2012). Compared to this global view, CNRM-ESM1 displays features that are broadly consistent with the CO_2^{ANTH} estimates. However, the stronger flow of NADW and AABW leads to a depletion of the stock of CO_2^{ANTH} between 0 and 1200 m (Fig. 16c). This mechanism leads to an increase in the stock of CO_2^{ANTH} at depth. Over the 1850–1994 period, the model takes up a total of 100.8 Pg C, which is in agreement with the observations that suggest a net uptake of 106 ± 17 Pg C over the same period (Khatiwala et al., 2013; Sabine et al., 2004).
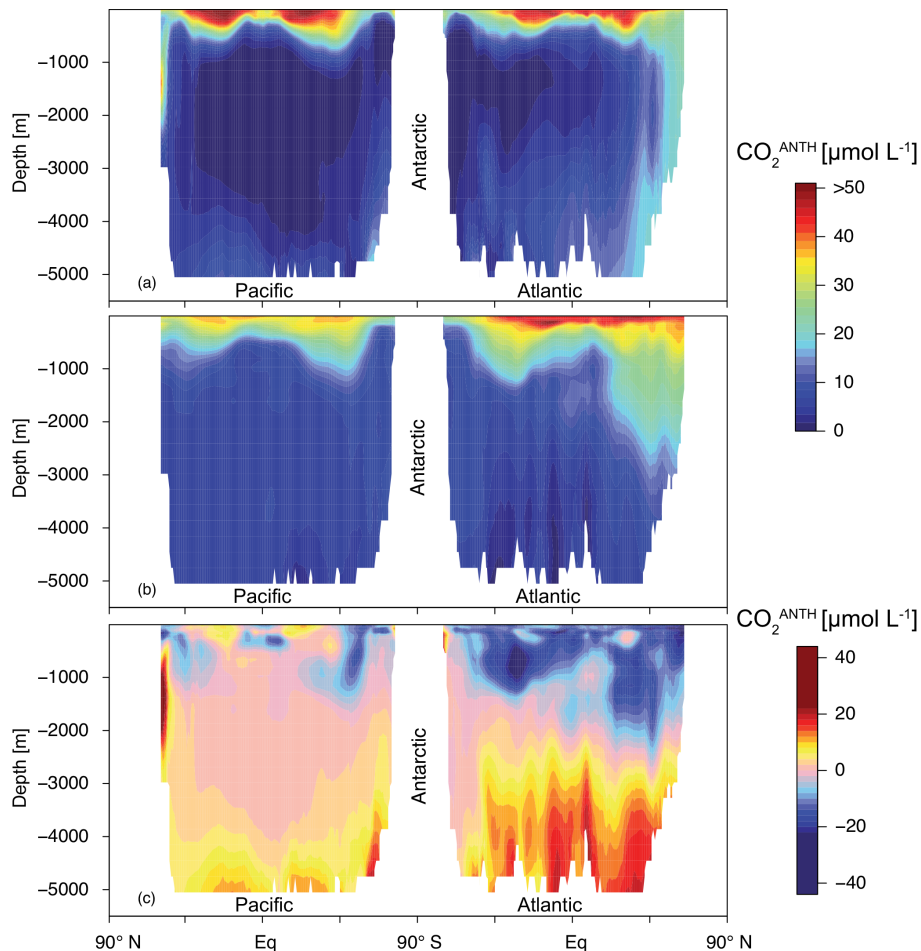
Figure 16. Annual-mean zonal-average anthropogenic carbon (CO_2^{ANTH}) across the Atlantic and Pacific oceans as simulated by CNRM-ESM1 averaged over 1990–2005 **(a)** and as estimated from the GLODAP database compiling data up to 1994 **(b)**. Panel **(c)** represents the mean-annual bias in zonal structures between model and observation-based estimates in CO_2^{ANTH}.

4.2.6   Ecosystem dynamics

In this section, we assess the performance of CNRM-ESM1 in terms of two ecosystem dynamics parameters, namely, the peak leaf area index (LAI_{max}) and the ocean surface chlorophyll (Chl). Both parameters have been monitored continuously from space since the 1980s and the 1990s, respectively, providing a suitable set of indirect observations to assess the simplified ecosystem representation embedded in Earth system models.

With regard to LAI_{max}, Fig. 17 shows that the model agrees well with satellite-derived observations (Zhu et al., 2013) except over Africa and Asia with overestimated values. As such, this ecosystem parameter behaves similarly to GPP and Ra, responding to biases in PR and PAR. In the northern mid-latitudes, LAI_{max} is slightly overestimated compared to the satellite-derived observations but remains in the low range of values simulated by other CMIP5 Earth system models evaluated in Anav et al. (2013b). Using an offline

simulation forced with atmospheric reanalyzes (Szczypta et al., 2014) shows similar biases in LAI over northern Europe as those noticed in CNRM-ESM1. It is thus likely that missing processes like forest and crop management or fire-induced disturbance might induce an overestimated LAI_{max}.

With regard to ocean Chl, Fig. 18 shows that CNRM-ESM1 displays a reasonable agreement with satellite-derived observations (O'Reilly et al., 1998). Although regional patterns of Chl concentrations were improved compared to that of CNRM-CM5 (Séférian et al., 2013), major model discrepancies are found in oligotrophic gyres and equatorial upwellings. Biases are more pronounced in the Southern Hemisphere where the model fails to produce very low Chl in the southern Pacific gyres. CNRM-ESM1 also fails at capturing western border high Chl concentrations in relation with the equatorial upwelling. Underestimated Chl concentrations in upwelling systems are essentially due to biases in surface wind forcing as well as to the coarse horizontal and vertical resolution of the ocean model. This model limitation
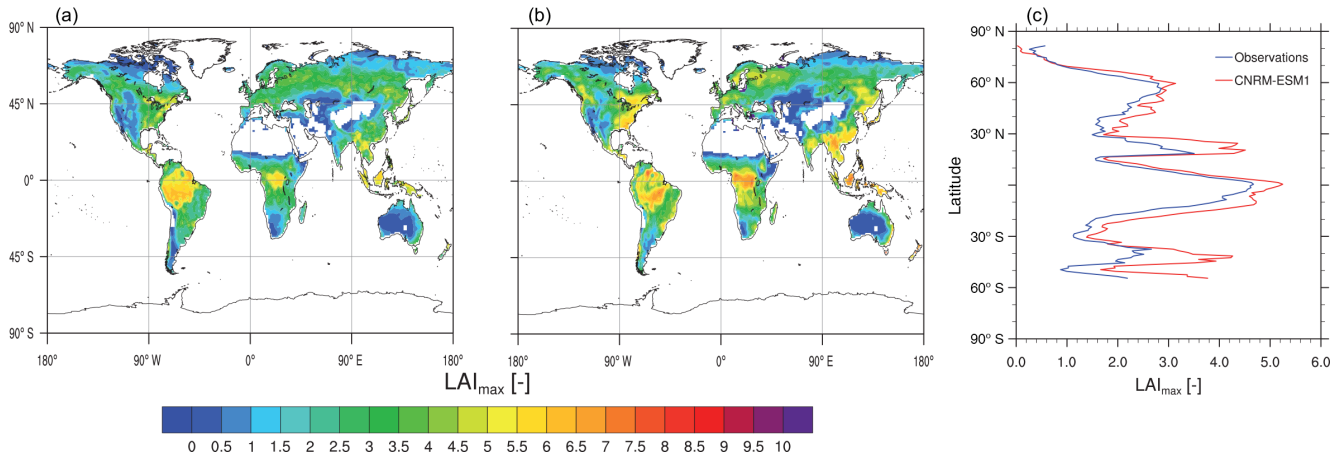
Figure 17. Composite of yearly maximum of leaf area index (LAI_{max}) as estimated from AVHRR satellite observations of Zhu et al. (2013) **(a)** and as simulated by CNRM-ESM1 **(b)** over 1986–2005. Panel **(c)** represents the zonal-average LAI_{max} in function of latitude for both observation-based estimates (in blue) and CNRM-ESM1 (in red).
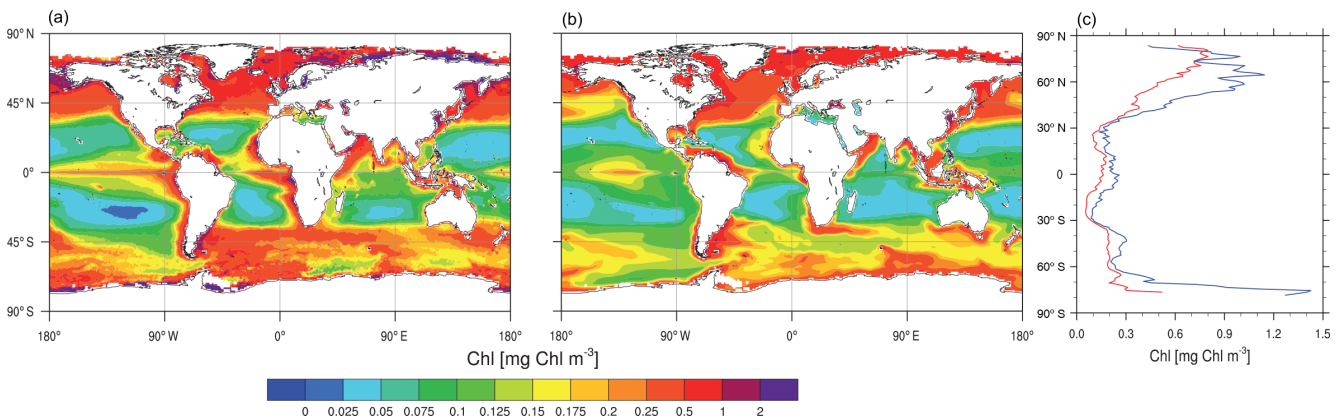
Figure 18. Annual-mean surface chlorophyll concentrations (Chl) as estimated from SeaWiFS over 1997–2010 **(a)** and as simulated by CNRM-ESM1 **(b)** over 1986–2005. Panel **(c)** represents the zonal-averaged Chl in function of latitude for both satellite-derived estimates (in blue) and CNRM-ESM1 (in red).

partly explains why Chl concentrations are underestimated in high-latitude oceans. In these domains, high coastal concentrations are captured from satellite sensors but cannot be resolved by the model due to its coarse resolution.

4.3 Recent evolution of the climate system

In the present section, we analyze the transient response of various climate indices to the recent climate forcing from 1901 to 2005. We focus on the near-surface temperature (T_{2m}), the September Arctic sea-ice extent (SIE), the 0–2000 m ocean heat content (OHC) as well as the land and ocean carbon sinks (LCS and OCS, respectively). Over this period, these climate indices are analyzed with their nominal values except for T_{2m} and OHC that are represented with respect to the 1961–1990 and the 1955–2005 periods, respectively. Figure 19 illustrates how these various climate indices evolve from 1901 to 2005 and Table 3 summarizes

their mean-state, interannual variability (IAV) and decadal trends over the 1986–2005 period.

Figure 19 shows that the transient response of T_{2m} agrees reasonably well with modern observations (Morice et al., 2012). At the end of the last decades of the historical simulation (i.e., 1986–2005), CNRM-ESM1 overestimates the T_{2m} increase, a discrepancy widely shared by other CMIP5 Earth system models (Huber and Knutti, 2014; Kosaka and Xie, 2013; Meehl et al., 2011; Watanabe et al., 2013). The amplitude of the simulated recent IAV is in line with the observations (Table 3). In particular, the model simulates strong cooling followed by stronger warming after the 1991 mount Pinatubo eruption. Contrasting with temperature, the simulated SIE poorly agrees with observation-based estimates (Cavalieri et al., 1996; Comiso, 1999; Rayner et al., 2003). Indeed, CNRM-ESM1 underestimates the mean-state SIE by about 2×10^6 km^2 and overestimates not only the IAV but
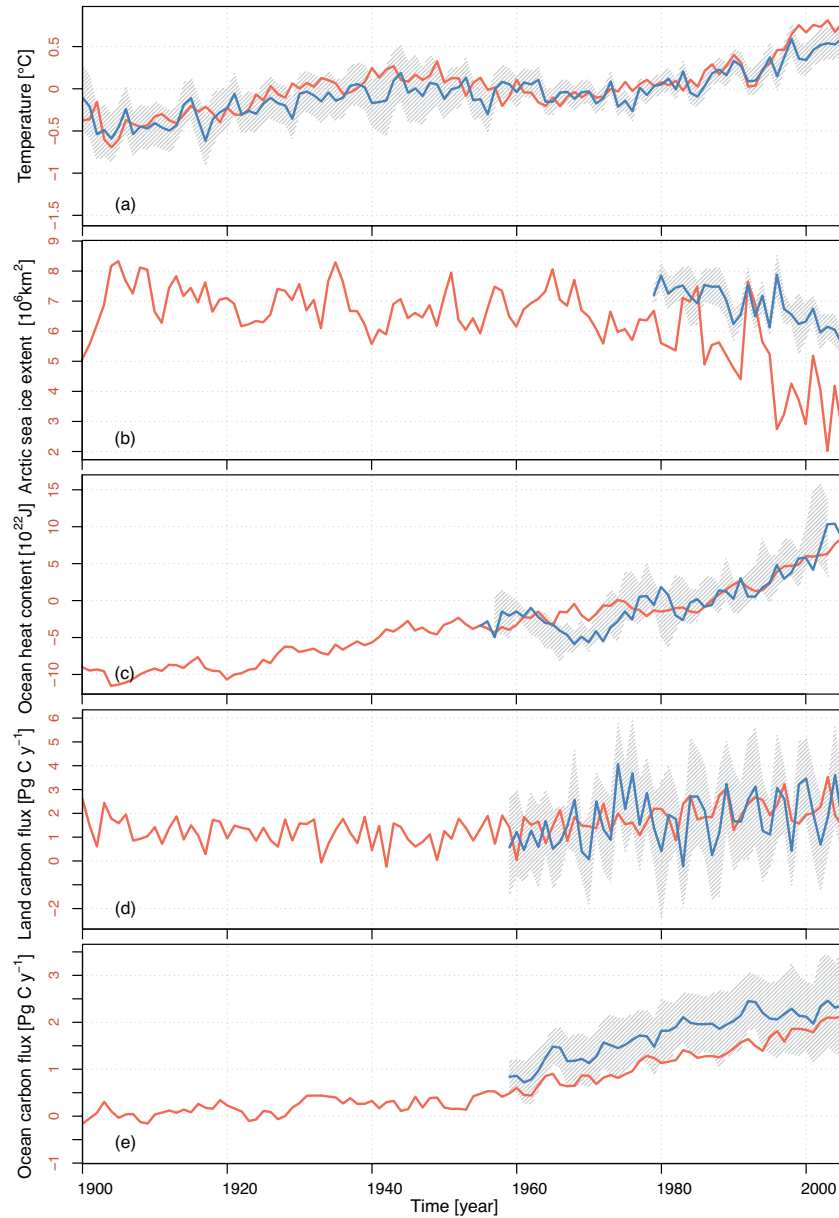
Figure 19. Time series of various climate indices as monitored from available observations (blue solid line) and as simulated by CNRM-ESM1 (red solid line) since 1901 with global near-surface temperature **(a)**, September Arctic sea-ice extent **(b)**, 0–2000 m ocean heat content **(c)**, land carbon flux **(d)** and ocean carbon flux **(e)**. Hatching represents the $\pm 2\sigma$ estimated from the ensemble deviation between the 100 members of the HadCRUT4 database (Morice et al., 2012) for near-surface temperature, the standard deviation between two National Snow and Ice Data Center estimates (Fetterer et al., 2002; Comiso, 1999) and Hadisst (Rayner et al., 2003) databases, the pentadal variability of the observed ocean heat content (Levitus et al., 2012) and spread between Global Carbon Project reconstructions for both land and ocean (Le Quéré et al., 2014). For both OCS and LCS, positive (negative) fluxes indicate an uptake (outgassing) of CO_2.

also the decadal decrease in extent (Table 3). Therefore, in terms of Arctic sea ice, the skill of CNRM-ESM1 is similar to CNRM-CM5 as detailed in Massonnet et al. (2012). A better agreement is found for OHC for which CNRM-ESM1 results agree with observation-based estimates in term of mean-state and decadal trends (Fig. 19, Table 3). Only the recent IAV in OHC is underestimated by the model, but the

latter is poorly constrained by the observations with regard to the small amount of data available below 1000 m (Levitus et al., 2012, 2009; Willis et al., 2004).

The recent evolution of LCS and OCS agrees with the range of observation-based and model-derived estimates (Le Quéré et al., 2014; Takahashi et al., 2010) with an uptake of CO_2 of about 2.1 and 1.7 Pg C year^{-1} for land and ocean,

Table 3. Modern mean-state, interannual variability (IAV) and decadal trends of various global climate indices: the near-surface temperature ($T_{2\,m}$), Arctic September sea-ice extent (SIE), 0–2000 m ocean heat content (OHC) as well as the land and ocean carbon sinks (LCS and OCS, respectively). For LCS and OCS, positive values indicate an uptake of CO_2 by land and ocean. All metrics are computed over the 1986–2005 period for both model and observations. Decadal trends are estimated from linear regression over the 1986–2005 period. IAV is estimated from the standard deviation of the detrended time series.

|		CNRM-ESM1	Observations
$T_{2\,m}$ [°C]	mean	0.43	0.30 ± 0.08 (Morice et al., 2012)
	IAV	0.13	0.10
	trend	4.0×10^{-2}	2.6×10^{-2}
SIE [$10^6\,km^2$]	mean	4.68	6.70 ± 0.26 (Comiso, 1999; Fetterer et al., 2002; Rayner et al., 2003)
	IAV	1.14	0.46
	decadal	-16×10^{-2}	-6.8×10^{-2}
OHC [$10^{22}\,J$]	mean	3.34	3.50 ± 1.42 (Levitus et al., 2012)
	IAV	0.69	1.43
	trend	0.44	0.50
LCS [$Pg\,C\,year^{-1}$]	mean	2.19	2.06 ± 1.0 [models] (Le Quéré et al., 2014)
			2.19 ± 0.8 [residual land carbon sink] (Friedlingstein et al., 2010)
	IAV	0.59	1.01
	trend	0.3×10^{-2}	1.8×10^{-2}
OCS [$Pg\,C\,year^{-1}$]	mean	1.65	1.87 ± 0.4 [models] (Le Quéré et al., 2014)
			2.15 ± 0.5 [obs.-models combination]
			2.0 ± 0.7 (Takahashi et al., 2010)
	IAV	0.09	0.14
	trend	4.5×10^{-2}	1.8×10^{-2}

respectively (Table 3). Underestimation in mean-state OCS is essentially due to the stronger river-induced offshore outgassing of CO_2, which is about $0.9\,Pg\,C\,year^{-1}$ in the model and assumed to be of $0.45\,Pg\,C\,year^{-1}$ in the observation-derived estimates. Both OCS and LCS IAV are underestimated in CNRM-ESM1 compared to the estimates. For OCS IAV, this behavior is found in most ocean biogeochemical models as shown in Wanninkhof et al. (2013). Indeed, simulated IAV from biogeochemical models substantially contrasts with the large IAV estimated from atmospheric inversion, which also contributes to the mix of observations and model reconstructions that compose the data (Le Quéré et al., 2014). For the land carbon cycle, underestimated LCS IAV may be related to the under-sensitivity of ISBA to climate variability in contrast with the over-sensitivity to the rising CO_2, a behavior shared with other land-surface process-based models (Piao et al., 2013). Note that differences in phase between simulated and estimated LCS were expected since the land sink of carbon is approximated from the difference between atmospheric growth rate, land use emissions and ocean carbon sink (Friedlingstein et al., 2010).

5   Summary and conclusions

In this article, we evaluate the ability of the Centre National de Recherches Météorologiques Earth system model version 1 (CNRM-ESM1) to reproduce the modern carbon cycle and its prominent physical drivers. CNRM-ESM1 derives from the atmosphere–ocean general circulation model CNRM-CM5 (Voldoire et al., 2013) that has contributed to CMIP5 and to the fifth IPCC assessment report. This model employs the same resolution and components as CNRM-CM5 although it uses updated versions of the atmospheric model (ARPEGE-CLIMAT v6.1), surface scheme (SURFEXv7.3) and sea-ice model (GELATO6) in addition to a 6 h coupling frequency. Several biophysical coupling processes are enabled in CNRM-ESM1 thanks to the terrestrial carbon cycle module ISBA (Gibelin et al., 2008) and the marine biogeochemistry module PISCES (Aumont and Bopp, 2006). They consist of the land biosphere-mediated evapotranspiration feedback and the ocean biota heat-trapping feedbacks.

Since an earlier version of CNRM-CM5 including the marine biogeochemistry module PISCES was distributed and used in several studies (Frölicher et al., 2014; Laufkötter et al., 2015; Schwinger et al., 2014; Séférian et al., 2013), the inclusion of the terrestrial carbon cycle module ISBA constitutes the major advancement in the CNRM-ESM1 development. Although the ISBA terrestrial carbon cycle module was developed at CNRM in the 2000s, it had never been coupled to an atmosphere–ocean model and run for long climate simulations. Here, we show that ISBA embedded in CNRM-ESM1 reproduces the general pattern of the vegetation and
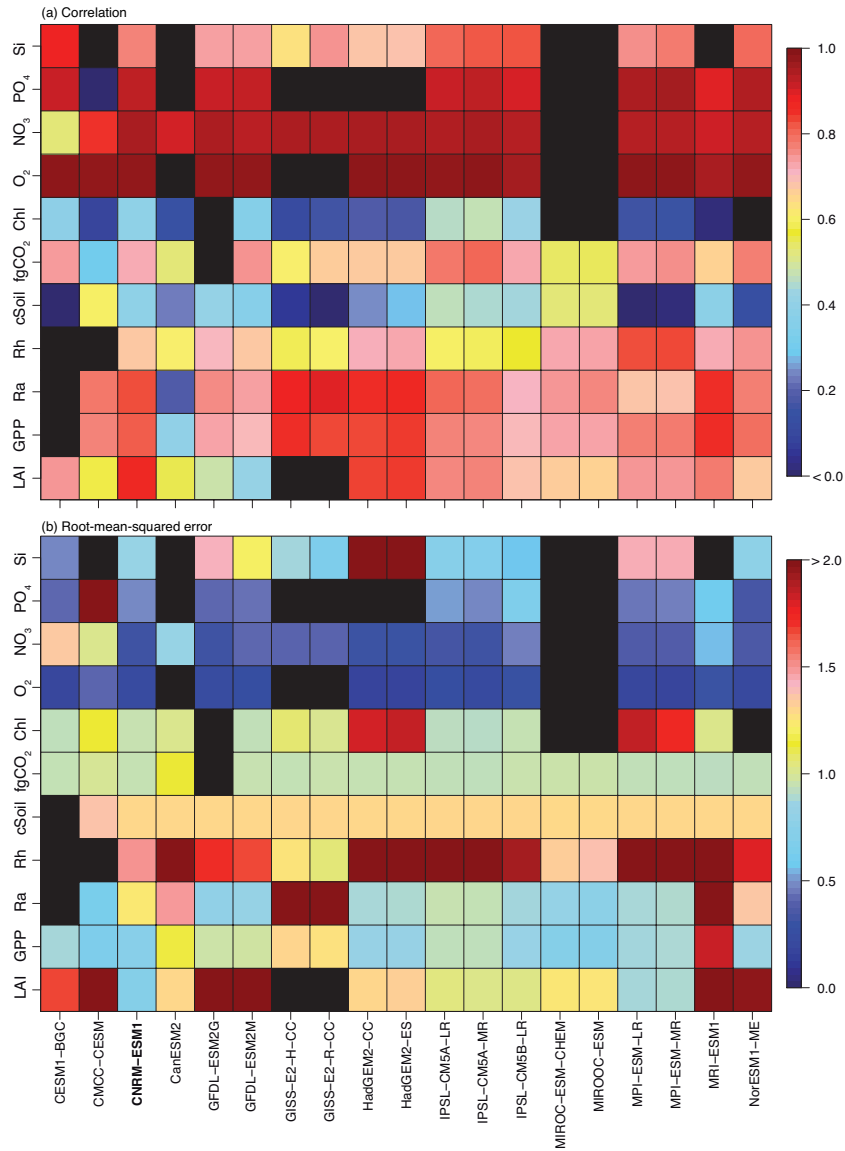
Figure 20. Skill-score matrix based on **(a)** spatial correlation and **(b)** globally averaged root mean squared error for relevant fields of the simulated carbon cycle from current generation Earth system models. Leaf area index (LAI), gross primary productivity (GPP), autotrophic respiration (Ra), heterotrophic respiration (Rh) and soil carbon (cSoil) are used to assess model skill in terms of modern mean-state terrestrial carbon cycle. Sea–air carbon flux (fgCO$_2$), surface chlorophyll (Chl) and surface concentrations of oxygen (O$_2$), nitrate (NO$_3$), phosphate (PO$_4$) and silicon (Si) are used to evaluate the skill of the current models at replicate modern mean-state ocean carbon cycle. Both models and observed fields are averaged over time from 1986 to 2005 to determine skill score metrics, except for cSoil, O$_2$, NO$_3$, PO$_4$, Si observations (only a modern mean-state climatology is available). Black squares indicate that models fields are not available (implying that these fields are either not simulated by the model or not published on the Earth System Grid Federation, ESGF).

soil carbon stock over the last decades. Although the photosynthesis scheme in ISBA differs from the other state-of-the-art process-based models (e.g., Dalmonech et al., 2014), the model displays similar behavior. That is, it overestimates both the land–vegetation gross primary productivity and the terrestrial ecosystem respiration. The compensation between these two fluxes leads to a correct land carbon sink over the modern period that agrees with the most up-to-date estimates

(Friedlingstein et al., 2010; Jung et al., 2011; Le Quéré et al., 2014). The largest model–data mismatch is found in the tropics where the gross uptake of CO$_2$ from the vegetation is strongly compensated by an overestimated autotrophic respiration. Maybe apart from this compensating mechanism, our analysis demonstrates that the terrestrial carbon cycle module of CNRM-ESM1 displays similar performances as other IPCC-class vegetation models (Figs. 20, S11 and S12;

see also details in Anav et al., 2013a, and Piao et al., 2013). The future effort in development will be oriented towards a better parameterization of the carbon absorption and respiration by the vegetation in association with a better representation of ecophysiological processes as detailed in Joetzjer et al. (2015). Further processes like fire-induced disturbance, mortality or linked with permafrost will also be included in order to improve the representation of the live biomass and soil carbon pool.

With regard to the marine biogeochemistry component, CNRM-ESM1 produces results in terms of biogeochemical variables that are comparable to other IPCC-class ocean biogeochemical models (Fig. 20). The global distribution of biogeochemical tracers such as oxygen, nutrients and carbon-related fields has been improved with respect to an earlier model version presented in Séférian et al. (2013) (Figs. 14 and S9). This change is attributed to a stronger northward flow of deep water masses from the Southern Ocean, which improves the vertical distribution of biogeochemical tracers. However, the strengthening of the meridional flow of deep water masses has also distorted the vertical structure of some carbon-related fields. Indeed, the unrealistic flow of North Atlantic deep water of about 26.1 Sv tends to deplete the stock of anthropogenic carbon storage between surface and 1200 m (Fig. 16c) and consequently to increase it at depth. Since biases in anthropogenic carbon storage compensate across the water column, the simulated anthropogenic carbon storage agrees with 1994 observation-based estimates. With regard to the ocean carbon sink, CNRM-ESM1 simulates a global ocean carbon sink that falls within the lower range of the combination of observation and model estimates over the recent years (Le Quéré et al., 2014). This slightly underestimated carbon sink is attributed to larger outgassing of natural CO_2 induced by the riverine input, which fits the upper range of values documented in the fifth IPCC assessment report (IPCC, 2013). Future development will target a better representation of this flux of carbon in close relationship with the recent development on the land-surface hydrology (Decharme et al., 2013).

We show that CNRM-ESM1 displays results comparable to those of CNRM-CM5 in spite of the inclusion of the global carbon cycle and various biophysical feedbacks. Simulated near-surface temperature, precipitation, incoming shortwave radiation over continents as well as temperature, salinity and mixed-layer depth over oceans broadly agree with observations or satellite-derived product. Except for the salinity and the mixed-layer depth, CNRM-ESM1 display quite similar skill at simulating physical drivers of the global carbon cycle compared to CNRM-CM5. Such a comparison demonstrates the reliability of this model to produce suitable simulations for future climate change projection and impacts studies.

In addition to preindustrial control and historical simulations discussed in this article, several other simulations were performed with CNRM-ESM1 following both the Coupled Model Intercomparison Project Phase 5 (CMIP5) and the Geoengineering Model Intercomparison Project (GeoMIP) experimental design. The CNRM-ESM1 model outputs (referred as "CNRM-ESM1") are available for download on Earth System Grid Federation (ESGF) under CMIP5 and GeoMIP projects.

Code availability

A number of model codes developed at CNRM, or in collaboration with CNRM scientists, is available as open-source code (see https://opensource.cnrm-game-meteo.fr/ and http://www.nemo-ocean.eu/). However, this is not the case for the Earth system model presented in this paper. Part of its code is nevertheless available upon request from the authors of the paper.

The Supplement related to this article is available online at doi:10.5194/gmd-9-1423-2016-supplement.

References

Adler, R. F., Huffman, G. J., Chang, A., Ferraro, R., Xie, P.-P., Janowiak, J., Rudolf, B., Schneider, U., Curtis, S., Bolvin, D., Gruber, A., Susskind, J., Arkin, P., and Nelkin, E.: The Version-2 Global Precipitation Climatology Project (GPCP) Monthly Precipitation Analysis (1979–Present), J. Hydrometeorol., 4, 1147–1167, doi:10.1175/1525-7541(2003)004<1147:TVGPCP>2.0.CO;2, 2003.

Ammann, C. M., Joos, F., Schimel, D. S., Otto-Bliesner, B. L., and Tomas, R. A.: Solar influence on climate during the past millennium: Results from transient simulations with the NCAR Climate System Model, Proc. Natl. Acad. Sci., 104, 3713–3718, doi:10.1073/pnas.0605064103, 2007.

Anav, A., Friedlingstein, P., Kidston, M., Bopp, L., Ciais, P., Cox, P., Jones, C., Jung, M., Myneni, R., and Zhu, Z.: Evaluating the Land and Ocean Components of the Global Carbon Cycle in the CMIP5 Earth System Models, J. Climate, 26, 6801–6843, doi:10.1175/JCLI-D-12-00417.1, 2013a.

Anav, A., Murray-Tortarolo, G., Friedlingstein, P., Sitch, S., Piao, S., and Zhu, Z.: Evaluation of Land Surface Models in Reproducing Satellite Derived Leaf Area Index over the High-Latitude

Northern Hemisphere. Part II: Earth System Models, Remote Sensing, 5, 3637–3661, doi:10.3390/rs5083637, 2013b.

Antonov, J. I., Locarnini, R., Boyer, T., Mishonov, A., Garcia, H., and Levitus, S.: World Ocean Atlas 2005 Volume 2: Salinity, NOAA Atlas NESDIS, 62, 2006.

Arora, V. K., Boer, G. J., Friedlingstein, P., Eby, M., Jones, C. D., Christian, J. R., Bonan, G., Bopp, L., Brovkin, V., Cadule, P., Hajima, T., Ilyina, T., Lindsay, K., Tjiputra, J. F., and Wu, T.: Carbon–Concentration and Carbon–Climate Feedbacks in CMIP5 Earth System Models, J. Climate, 26, 5289–5314, doi:10.1175/JCLI-D-12-00494.1, 2013.

Aumont, O. and Bopp, L.: Globalizing results from ocean in situ iron fertilization studies, Global Biogeochem. Cy., 20, GB2017, doi:10.1029/2005GB002591, 2006.

Aumont, O., Maier-Reimer, E., Blain, S., and Monfray, P.: An ecosystem model of the global ocean including Fe, Si, P colimitations, Global Biogeochem. Cy., 17, 1060, doi:10.1029/2001GB001745, 2003.

Axell, L.: Wind-driven internal waves and Langmuir circulations in a numerical ocean model of the southern Baltic Sea, J. Geophys. Res.-Ocean., 107, 3204, doi:10.1029/2001JC000922, 2002.

Barnier, B., Madec, G., Penduff, T., Molines, J.-M., Treguier, A.-M., Sommer, J., Beckmann, A., Biastoch, A., Böning, C., Dengg, J., Derval, C., Durand, E., Gulev, S., Remy, E., Talandier, C., Theetten, S., Maltrud, M., McClean, J., and Cuevas, B.: Impact of partial steps and momentum advection schemes in a global ocean circulation model at eddy-permitting resolution, Ocean Dynam., 56, 543–567, doi:10.1007/s10236-006-0082-1, 2006.

Battin, T. J., Luyssaert, S., Kaplan, L. A., Aufdenkampe, A. K., Richter, A., and Tranvik, L. J.: The boundless carbon cycle, Nat. Geosci., 2, 598–600, doi:10.1038/ngeo618, 2009.

Blanke, B. and Delecluse, P.: Variability of the Tropical Atlantic Ocean Simulated by a General Circulation Model with Two Different Mixed-Layer Physics, J. Phys. Oceanogr., 23 1363–1388, doi:10.1175/1520-0485(1993)023<1363:VOTTAO>2.0.CO;2, 1993.

Boone, A., Calvet, J.-C., and Noilhan, J.: Inclusion of a Third Soil Layer in a Land Surface Scheme Using the Force–Restore Method, J. Appl. Meteor., 38, 1611–1630, doi:10.1175/1520-0450(1999)038<1611:IOATSL>2.0.CO;2, 1999.

Bouillon, S., Morales Maqueda, M. Á., Legat, V., and Fichefet, T.: An elastic–viscous–plastic sea ice model formulated on Arakawa B and C grids, Ocean Model., 27, 174–184, 2009.

Bretherton, F. P.: Earth system science and remote sensing, Proc. IEEE, 73, 1118–1127, doi:10.1109/PROC.1985.13242, 1985.

Calvet, J.-C.: Investigating soil and atmospheric plant water stress using physiological and micrometeorological data, Agr. Forest Meteorol., 103, 229–247, 2000.

Calvet, J.-C. and Soussana, J.-F.: Modelling CO_2-enrichment effects using an interactive vegetation SVAT scheme, Agr. Forest Meteorol., 108, 129–152, doi:10.1016/S0168-1923(01)00235-0, 2001.

Calvet, J.-C., Noilhan, J., Roujean, J.-L., Bessemoulin, P., Cabelguenne, M., Olioso, A., and Wigneron, J.-P.: An interactive vegetation SVAT model tested against data from six contrasting sites, Agr. Forest Meteorol., 92, 73–95, doi:10.1016/S0168-1923(98)00091-4, 1998.

Calvet, J.-C., Rivalland, V., Picon-Cochard, C., and Guehl, J.-M.: Modelling forest transpiration and CO_2 fluxes—response to soil moisture stress, Agr. Forest Meteorol., 124, 143–156, 2004.

Calvet, J.-C., Gibelin, A.-L., Roujean, J.-L., Martin, E., Le Moigne, P., Douville, H., and Noilhan, J.: Past and future scenarios of the effect of carbon dioxide on plant growth and transpiration for three vegetation types of southwestern France, Atmos. Chem. Phys., 8, 397–406, doi:10.5194/acp-8-397-2008, 2008.

Cariolle, D. and Brard, D.: The Distribution of Ozone and Active Stratospheric Species: Results of a Two-Dimensional Atmospheric Model, in: Atmospheric Ozone, edited by: Zerefos, C. S. and Ghazi, A., Springer Netherlands, 77–81, 1985.

Cariolle, D. and Teyssèdre, H.: A revised linear ozone photochemistry parameterization for use in transport and general circulation models: multi-annual simulations, Atmos. Chem. Phys., 7, 2183–2196, doi:10.5194/acp-7-2183-2007, 2007.

Carrer, D., Ceamanos, X., and Roujean, J. L.: Analysis of snow-free vegetation and bare soil albedos and application to numerical weather prediction, 2013 IEEE International Geoscience and Remote Sensing Symposium – IGARSS, 21–26 July 2013 , Melbourne, VIC, Australia, 3789–3792, doi:10.1109/IGARSS.2013.6723656, 2013a.

Carrer, D., Roujean, J. L., Lafont, S., Calvet, J.-C., Boone, A., Decharme, B., Delire, C., and Gastellu-Etchegorry, J. P.: A canopy radiative transfer scheme with explicit FAPAR for the interactive vegetation model ISBA-A-gs: Impact on carbon fluxes, J. Geophys. Res.-Biogeo., 118, 888–903, doi:10.1002/jgrg.20070, 2013b.

Cavalieri, D. J., Parkinson, C. L., Gloersen, P., and Zwally, H.: Sea Ice Concentrations from Nimbus-7 SMMR and DMSP SSM/I-SSMIS Passive Microwave Data, years 1978–2014, Boulder, Colorado USA: NASA DAAC at the National Snow and Ice Data Center, 1996.

Collatz, G. J., Ribas-Carbo, M., and Berry, J. A.: Coupled Photosynthesis-Stomatal Conductance Model for Leaves of C4 Plants, Funct. Plant Biol., 19, 519–538, 1992.

Comiso, J. C.: Bootstrap Sea Ice Concentrations from Nimbus-7 SMMR and DMSP SSM/I-SSMIS (Version 2), 2nd Edn., Boulder, Colorado USA: National Snow and Ice Data Center., 1999.

Cox, P., Betts, R., Jones, C., Spall, S., and Totterdell, I.: Acceleration of global warming due to carbon-cycle feedbacks in a coupled climate model, Nature, 408, 184–187, 2000.

Dalmonech, D., Foley, A. M., Anav, A., Friedlingstein, P., Friend, A. D., Kidston, M., Willeit, M., and Zaehle, S.: Challenges and opportunities to reduce uncertainty in projections of future atmospheric CO_2: a combined marine and terrestrial biosphere perspective, Biogeosciences Discuss., 11, 2083–2153, doi:10.5194/bgd-11-2083-2014, 2014.

de Baar, H. J. W. and de Jong, J. T. M.: The biogeochemistry of iron in seawater, edited by: Turner, D. R. and Hunter, K. A., John Wiley, Hoboken, N. J., 2001.

Decharme, B., Martin, E., and Faroux, S.: Reconciling soil thermal and hydrological lower boundary conditions in land surface models, J. Geophys. Res.-Atmos., 118, 7819–7834, doi:10.1002/jgrd.50631, 2013.

DeFries, R. S., Field, C. B., Fung, I., Collatz, G. J., and Bounoua, L.: Combining satellite data and biogeochemical models to estimate global effects of human-induced land cover change on

carbon emissions and primary productivity, Global Biogeochem. Cy., 13, 803–815, doi:10.1029/1999GB900037, 1999.

de Lavergne, C., Palter, J. B., Galbraith, E. D., Bernardello, R., and Marinov, I.: Cessation of deep convection in the open Southern Ocean under anthropogenic climate change, Nature Clim. Change, 4, 278–282, doi:10.1038/nclimate2132, 2014.

Douville, H., Royer, J. F., and Mahfouf, J. F.: A new snow parameterization for the Météo-France climate model, Clim. Dynam., 12, 21–35, doi:10.1007/BF00208760, 1995.

Eppley, R. W., Rogers, J. N., and McCarthy, J. J.: Half-Saturation Constants for Uptake of Nitrate and Ammonium by Marine Phytoplankton, Limnol. Oceanogr., 14, 912–920, doi:10.4319/lo.1969.14.6.0912, 1969.

Eyring, V., Arblaster, J. M., and Cionni, I.: Long-term ozone changes and associated climate impacts in CMIP5 simulations, J. Geophys. Res.-Atmos., 118, 5029–5060, doi:10.1002/jgrd.50316, 2013.

Fairall, C. W., Bradley, E. F., Hare, J. E., Grachev, A. A., and Edson, J. B.: Bulk Parameterization of Air–Sea Fluxes: Updates and Verification for the COARE Algorithm, J. Climate, 16, 571–591, doi:10.1175/1520-0442(2003)016<0571:BPOASF>2.0.CO;2, 2003.

FAO/IIASA/ISRIC/ISSCAS/JRC: Harmonized World Soil Database (version 1.10), FAO, Rome, Italy and IIASA, Laxenburg, Austria, 2012.

Farquhar, G. D., Caemmerer, S., and Berry, J. A.: A biochemical model of photosynthetic CO_2 assimilation in leaves of C3 species, Planta, 149, 78–90, doi:10.1007/BF00386231, 1980.

Fetterer, F., Knowles, K., Meier, W., and Savoie, M.: Sea Ice Index, 2014 Edn., Boulder, Colorado USA: National Snow and Ice Data Center, available at: doi:10.7265/N5QJ7F7W, 2002.

Flato, G. M.: Earth system models: an overview, WIREs Clim. Change, 2, 783–800, doi:10.1002/wcc.148, 2011.

Friedlingstein, P. and Prentice, I. C.: Carbon-climate feedbacks: a review of model and observation based estimates, Current Opinion in Environmental Sustainability, 2, 251–257, doi:10.1016/j.cosust.2010.06.002, 2010.

Friedlingstein, P., Houghton, R. A., Marland, G., Hackler, J., Boden, T. A., Conway, T. J., Canadell, J. G., Raupach, M. R., Ciais, P., and Le Quéré, C.: Update of CO_2 emissions, Naturego, Nature Publishing Group, 3, 811–812, doi:10.1038/ngeo1022, 2010.

Friedlingstein, P., Meinshausen, M., Arora, V. K., Jones, C. D., Anav, A., Liddicoat, S. K., and Knutti, R.: Uncertainties in CMIP5 climate projections due to carbon cycle feedbacks, J. Climate, 27, 511–526, doi:10.1175/JCLI-D-12-00579.1, 2013.

Frölicher, T. L., Sarmiento, J. L., Paynter, D. J., Dunne, J. P., Krasting, J. P., and Winton, M.: Dominance of the Southern Ocean in anthropogenic carbon and heat uptake in CMIP5 models, J. Climate, 28, 862–886, doi:10.1175/JCLI-D-14-00117.1, 2014.

Geider, R., MacIntyre, H., and Kana, T.: A dynamic regulatory model of phytoplanktonic acclimation to light, nutrients, and temperature, Limnology and Oceanography, 43(4), 679–694, 1998.

Gibelin, A.-L., Calvet, J.-C., Roujean, J.-L., Jarlan, L., and Los, S. O.: Ability of the land surface model ISBA-A-gs to simulate leaf area index at the global scale: Comparison with satellites products, J. Geophys. Res., 111, D18102, doi:10.1029/2005JD006691, 2006.

Gibelin, A.-L., Calvet, J.-C., and Viovy, N.: Modelling energy and CO_2 fluxes with an interactive vegetation land surface model-Evaluation at high and middle latitudes, Agr. Forest Meteorol., 148, 1611–1628, doi:10.1016/j.agrformet.2008.05.013, 2008.

Goudriaan, J., van Laar, H. H., van Keulen, H., and Louwerse, W.: Photosynthesis, CO_2 and Plant Production, in: NATO ASI Science, edited by: Day, W. and Atkin, R. K., Springer US, Boston, MA, 86, 107–122, 1985.

Hajima, T., Kawamiya, M., Watanabe, M., Kato, E., Tachiiri, K., Sugiyama, M., Watanabe, S., Okajima, H., and Ito, A.: Modeling in Earth system science up to and beyond IPCC AR5, Progress in Earth and Planetary Science, 1, 29–25, doi:10.1186/s40645-014-0029-y, 2014.

Harris, I., Jones, P. D., Osborn, T. J., and Lister, D. H.: Updated high-resolution grids of monthly climatic observations – the CRU TS3.10 Dataset, Int. J. Climatol., 34, 623–642, doi:10.1002/joc.3711, 2013.

Heuzé, C., Heywood, K. J., Stevens, D. P., and Ridley, J. K.: Southern Ocean bottom water characteristics in CMIP5 models, Geophys. Res. Lett., 40, 1409–1414, doi:10.1002/grl.50287, 2013.

Houghton, R. A.: Balancing the Global Carbon Budget, Annu. Rev. Earth Pl. Sc., 35, 313–347, doi:10.1146/annurev.earth.35.031306.140057, 2007.

Huber, M. and Knutti, R.: Natural variability, radiative forcing and climate response in the recent hiatus reconciled, Nat. Geosci., 7, 651–656, doi:10.1038/ngeo2228, 2014.

Hunke, E. C. and Dukowicz, J. K.: An Elastic–Viscous–Plastic Model for Sea Ice Dynamics, J. Phys. Oceanogr., 27, 1849–1867, doi:10.1175/1520-0485(1997)027<1849:AEVPMF>2.0.CO;2, 1997.

IPCC: Climate Change 2007: The Physical Science Basis, edited by: Solomon, S., Qin, D., Manning, M., Chen, Z., Marquis, M., Averyt, K. B., Tignor, M., and Miller, H. L., Cambridge University Press, Cambridge, United Kingdom and New York, NY, USA, 2007.

IPCC: Climate Change 2013: The Physical Science Basis, edited by: Stoker, T. F., Qin, D., Plattner, G., Tignor, M., Allen, S. K., Boschung, J., Nauels, A., Xia, Y., Bex, V., and Midgley, P. M., Cambridge Univ Press, Cambridge, United Kingdom and New York, NY, USA, 2013.

Jacobs, C. M. J., van den Hurk, B. M. M., and de Bruin, H. A. R.: Stomatal behaviour and photosynthetic rate of unstressed grapevines in semi-arid conditions, Agr. Forest Meteorol., 80, 111–134, 1996.

Jacobson, A. R., Mikaloff Fletcher, S. E., Gruber, N., Sarmiento, J. L., and Gloor, M.: A joint atmosphere-ocean inversion for surface fluxes of carbon dioxide: 1. Methods and global-scale fluxes, Global Biogeochem. Cy., 21, GB1019, doi:10.1029/2005GB002556, 2007.

Jickells, T. and Spokes, L.: The biogeochemistry of iron in seawater, edited by D. R. Turner and K. A. Hunter, John Wiley, Hoboken, N. J., 2001.

Joetzjer, E., Delire, C., Douville, H., Ciais, P., Decharme, B., Fisher, R., Christoffersen, B., Calvet, J. C., da Costa, A. C. L., Ferreira, L. V., and Meir, P.: Predicting the response of the Amazon rainforest to persistent drought conditions under current and future climates: a major challenge for global land surface models, Geosci. Model Dev., 7, 2933–2950, doi:10.5194/gmd-7-2933-2014, 2014.

Joetzjer, E., Delire, C., Douville, H., Ciais, P., Decharme, B., Carrer, D., Verbeeck, H., De Weirdt, M., and Bonal, D.: Improving the ISBACC land surface model simulation of water and carbon fluxes and stocks over the Amazon forest, Geosci. Model Dev., 8, 1709–1727, doi:10.5194/gmd-8-1709-2015, 2015.

Johns, W. E., Baringer, M. O., Beal, L. M., Cunningham, S. A., Kanzow, T., Bryden, H. L., Hirschi, J. J. M., Marotzke, J., Meinen, C. S., Shaw, B., and Curry, R.: Continuous, Array-Based Estimates of Atlantic Ocean Heat Transport at 26.5° N, J. Climate, 24, 2429–2449, doi:10.1175/2010JCLI3997.1, 2011.

Johnson, K., Chavez, F., and Friederich, G.: Continental-shelf sediment as a primary source of iron for coastal phytoplankton, Nature, 398, 697–700, 1999.

Jung, M., Reichstein, M., Margolis, H. A., Cescatti, A., Richardson, A. D., Arain, M. A., Arneth, A., Bernhofer, C., Bonal, D., Chen, J., Gianelle, D., Gobron, N., Kiely, G., Kutsch, W., Lasslop, G., Law, B. E., Lindroth, A., Merbold, L., Montagnani, L., Moors, E. J., Papale, D., Sottocornola, M., Vaccari, F., and Williams, C.: Global patterns of land-atmosphere fluxes of carbon dioxide, latent heat, and sensible heat derived from eddy covariance, satellite, and meteorological observations, J. Geophys. Res., 116, G00J07, doi:10.1029/2010JG001566, 2011.

Key, R., Kozyr, A., Sabine, C., Lee, K., Wanninkhof, R., Bullister, J., Feely, R., Millero, F., Mordy, C., and Peng, T.: A global ocean carbon climatology: Results from Global Data Analysis Project (GLODAP), Global Biogeochem. Cy., 18, GB4031, doi:10.1029/2004GB002247, 2004.

Khatiwala, S., Tanhua, T., Mikaloff Fletcher, S., Gerber, M., Doney, S. C., Graven, H. D., Gruber, N., McKinley, G. A., Murata, A., Ríos, A. F., and Sabine, C. L.: Global ocean storage of anthropogenic carbon, Biogeosciences, 10, 2169–2191, doi:10.5194/bg-10-2169-2013, 2013.

Koch-Larrouy, A., Madec, G., Bouruet-Aubertot, P., Gerkema, T., Bessières, L., and Molcard, R.: On the transformation of Pacific Water into Indonesian Throughflow Water by internal tidal mixing, Geophys. Res. Lett., 34, L04604, doi:10.1029/2006GL028405, 2007.

Koch-Larrouy, A., Lengaigne, M., Terray, P., Madec, G., and Masson, S.: Tidal mixing in the Indonesian Seas and its effect on the tropical climate system, Clim. Dynam., 34, 891–904, doi:10.1007/s00382-009-0642-4, 2010.

Kosaka, Y. and Xie, S.-P.: Recent global-warming hiatus tied to equatorial Pacific surface cooling, Nature, 501, 403–407, doi:10.1038/nature12534, 2013.

Krinner, G., Viovy, N., de Noblet-Ducoudré, N., Ogée, J., Polcher, J., Friedlingstein, P., Ciais, P., Sitch, S., and Prentice, I. C.: A dynamic global vegetation model for studies of the coupled atmosphere-biosphere system, Global Biogeochem. Cy., 19, 1–33, 2005.

Landschützer, P., Gruber, N., Bakker, D. C. E., and Schuster, U.: Recent variability of the global ocean carbon sink, Global Biogeochem. Cy., 2014, GB004853, doi:10.1002/2014GB004853, 2014.

Laufkötter, C., Vogt, M., Gruber, N., Aita-Noguchi, M., Aumont, O., Bopp, L., Buitenhuis, E., Doney, S. C., Dunne, J., Hashioka, T., Hauck, J., Hirata, T., John, J., Le Quéré, C., Lima, I. D., Nakano, H., Seferian, R., Totterdell, I., Vichi, M., and Völker, C.: Drivers and uncertainties of future global marine primary pro-

duction in marine ecosystem models, Biogeosciences, 12, 6955–6984, doi:10.5194/bg-12-6955-2015, 2015.

Lengaigne, M., Madec, G., Bopp, L., Menkes, C., Aumont, O., and Cadule, P.: Bio-physical feedbacks in the Arctic Ocean using an Earth system model, Geophys. Res. Lett., 36, L21602, doi:10.1029/2009GL040145, 2009.

Lengaigne, M., Menkes, C., Aumont, O., Gorgues, T., Bopp, L., André, J.-M., and Madec, G.: Influence of the oceanic biology on the tropical Pacific climate in a coupled general circulation model, Clim. Dynam., 28, 503–516, doi:10.1007/s00382-006-0200-2, 2006.

Le Quéré, C., Andres, R. J., Boden, T., Conway, T., Houghton, R. A., House, J. I., Marland, G., Peters, G. P., van der Werf, G. R., Ahlström, A., Andrew, R. M., Bopp, L., Canadell, J. G., Ciais, P., Doney, S. C., Enright, C., Friedlingstein, P., Huntingford, C., Jain, A. K., Jourdain, C., Kato, E., Keeling, R. F., Klein Goldewijk, K., Levis, S., Levy, P., Lomas, M., Poulter, B., Raupach, M. R., Schwinger, J., Sitch, S., Stocker, B. D., Viovy, N., Zaehle, S., and Zeng, N.: The global carbon budget 1959–2011, Earth Syst. Sci. Data, 5, 165–185, doi:10.5194/essd-5-165-2013, 2013.

Le Quéré, C., Moriarty, R., Andrew, R. M., Peters, G. P., Ciais, P., Friedlingstein, P., Jones, S. D., Sitch, S., Tans, P., Arneth, A., Boden, T. A., Bopp, L., Bozec, Y., Canadell, J. G., Chini, L. P., Chevallier, F., Cosca, C. E., Harris, I., Hoppema, M., Houghton, R. A., House, J. I., Jain, A. K., Johannessen, T., Kato, E., Keeling, R. F., Kitidis, V., Klein Goldewijk, K., Koven, C., Landa, C. S., Landschützer, P., Lenton, A., Lima, I. D., Marland, G., Mathis, J. T., Metzl, N., Nojiri, Y., Olsen, A., Ono, T., Peng, S., Peters, W., Pfeil, B., Poulter, B., Raupach, M. R., Regnier, P., Rödenbeck, C., Saito, S., Salisbury, J. E., Schuster, U., Schwinger, J., Séférian, R., Segschneider, J., Steinhoff, T., Stocker, B. D., Sutton, A. J., Takahashi, T., Tilbrook, B., van der Werf, G. R., Viovy, N., Wang, Y.-P., Wanninkhof, R., Wiltshire, A., and Zeng, N.: Global carbon budget 2014, Earth Syst. Sci. Data, 7, 47–85, doi:10.5194/essd-7-47-2015, 2015.

Levitus, S., Conkright, M. E., Reid, J. L., Najjar, R. G., and Mantyla, A.: Distribution of nitrate, phosphate and silicate in the world oceans, Prog. Oceanogr., 31, 245–273, 1993.

Levitus, S., Antonov, J. I., Boyer, T. P., Locarnini, R. A., Garcia, H. E., and Mishonov, A. V.: Global ocean heat content 1955–2008 in light of recently revealed instrumentation problems, Geophys. Res. Lett., 36, L07608, doi:10.1029/2008GL037155, 2009.

Levitus, S., Antonov, J. I., Boyer, T. P., Baranova, O. K., Garcia, H. E., Locarnini, R. A., Mishonov, A. V., Reagan, J. R., Seidov, D., Yarosh, E. S., and Zweng, M. M.: World ocean heat content and thermosteric sea level change (0–2000 m), 1955–2010, Geophys. Res. Lett., 39, L10603, doi:10.1029/2012GL051106, 2012.

Levitus, S., Antonov, J. I., Baranova, O. K., Boyer, T. P., Coleman, C. L., Garcia, H. E., Grodsky, A. I., Johnson, D. R., Locarnini, R. A., Mishonov, A. V., Reagan, J. R., Sazama, C. L., Seidov, D., Smolyar, I., Yarosh, E. S., and Zweng, M. M.: The World Ocean Database TI, Data Science Journal, 12, WDS229–WDS234, 2013.

Lipschultz, F., Wofsy, S. C., Ward, B. B., Codispoti, L. A., Friedrich, G., and Elkins, J. W.: Bacterial transformations of inorganic nitrogen in the oxygen-deficient waters of the Eastern Tropical South Pacific Ocean, Deep-Sea Res., 37, 1513–1541, doi:10.1016/0198-0149(90)90060-9, 1990.

Locarnini, R. A., Mishonov, A. V., Antonov, J. I., Boyer, T. P., Garcia, H. E., Baranova, O. K., Zweng, M. M., and Johnson, D. R.: World Ocean Atlas 2005 Volume 1: Temperature, 2006.

Ludwig, W., Probst, J., and Kempe, S.: Predicting the oceanic input of organic carbon by continental erosion, Global Biogeochem. Cy., 10, 23–41, 1996.

Madec, G.: NEMO ocean engine, Institut Pierre-Simon Laplace (IPSL), France, Institut Pierre-Simon Laplace (IPSL), available at: http://www.nemo-ocean.eu/About-NEMO/ Reference-manuals (last access: November 2013), 2008.

Maier-Reimer, E.: Geochemical cycles in an ocean general circulation model. Preindustrial tracer distributions, Global Biogeochem. Cy., 7, 645, doi:10.1029/93GB01355, 1993.

Majkut, J. D., Sarmiento, J. L., and Rodgers, K. B.: A Growing Oceanic Carbon Uptake: Results from an inversion study of surface pCO$_2$ data, Global Biogeochem. Cy., 2013, GB004585, doi:10.1002/2013GB004585, 2014.

Masson, V., Champeaux, J.-L., Chauvin, F., Meriguet, C., and Lacaze, R.: A Global Database of Land Surface Parameters at 1-km Resolution in Meteorological and Climate Models, J. Climate, 16, 1261–1282, doi:10.1175/1520-0442(2003)16<1261:AGDOLS>2.0.CO;2, 2013a.

Masson, V., Le Moigne, P., Martin, E., Faroux, S., Alias, A., Alkama, R., Belamari, S., Barbu, A., Boone, A., Bouyssel, F., Brousseau, P., Brun, E., Calvet, J.-C., Carrer, D., Decharme, B., Delire, C., Donier, S., Essaouini, K., Gibelin, A.-L., Giordani, H., Habets, F., Jidane, M., Kerdraon, G., Kourzeneva, E., Lafaysse, M., Lafont, S., Lebeaupin Brossier, C., Lemonsu, A., Mahfouf, J.-F., Marguinaud, P., Mokhtari, M., Morin, S., Pigeon, G., Salgado, R., Seity, Y., Taillefer, F., Tanguy, G., Tulet, P., Vincendon, B., Vionnet, V., and Voldoire, A.: The SURFEXv7.2 land and ocean surface platform for coupled or offline simulation of earth surface variables and fluxes, Geosci. Model Dev., 6, 929–960, doi:10.5194/gmd-6-929-2013, 2013b.

Massonnet, F., Fichefet, T., Goosse, H., Bitz, C. M., Philippon-Berthier, G., Holland, M. M., and Barriat, P.-Y.: Constraining projections of summer Arctic sea ice, The Cryosphere, 6, 1383–1394, doi:10.5194/tc-6-1383-2012, 2012.

Meehl, G. A., Arblaster, J. M., Fasullo, J. T., Hu, A., and Trenberth, K. E.: Model-based evidence of deep-ocean heat uptake during surface-temperature hiatus periods, Nature Clim. Change, 1, 360–364, doi:10.1038/nclimate1229, 2011.

Mellor, G. and Blumberg, A.: Wave Breaking and Ocean Surface Layer Thermal Response, J. Phys. Oceanogr., 34, 693–698, doi:10.1175/2517.1, 2004.

Merryfield, W., Holloway, G., and Gargett, A.: A global ocean model with double-diffusive mixing, J. Phys. Oceanogr., 29, 1124–1142, 1999.

Middelburg, J., Soetaert, K., Herman, P., and Heip, C.: Denitrification in marine sediments: A model study, Global Biogeochem. Cy., 10, 661–673, 1996.

Mignot, J., Swingedouw, D., Deshayes, J., Marti, O., Talandier, C., Séférian, R., Lengaigne, M., and Madec, G.: On the evolution of the oceanic component of the IPSL climate models from CMIP3 to CMIP5: A mean state comparison, Ocean Model., 72, 167–184, doi:10.1016/j.ocemod.2013.09.001, 2013.

Mikaloff Fletcher, S. E., Gruber, N., Jacobson, A. R., Gloor, M., Doney, S. C., Dutkiewicz, S., Gerber, M., Follows, M., Joos, F., Lindsay, K., Menemenlis, D., Mouchet, A.,

Müller, S. A., and Sarmiento, J. L.: Inverse estimates of the oceanic sources and sinks of natural CO$_2$ and the implied oceanic carbon transport, Global Biogeochem. Cy., 21, GB1010, doi:10.1029/2006GB002751, 2007.

Monod, J.: Recherches sur la croissance des cultures bactériennes, Hermann, Paris, 1942.

Moore, J., Doney, S., Kleypas, J., Glover, D., and Fung, I.: An intermediate complexity marine ecosystem model for the global domain, Deep Sea Res. Pt. II, 49, 403–462, 2002.

Moore, J., Doney, S., and Lindsay, K.: Upper ocean ecosystem dynamics and iron cycling in a global three-dimensional model, Global Biogeochem. Cy., 18, GB4028, doi:10.1029/2004GB002220, 2004.

Morel, A.: Optical Modeling of the Upper Ocean in Relation to Its Biogenous Matter Content (Case-I Waters), J. Geophys. Res.-Oceans, 93, 10749–10768, 1988.

Morice, C. P., Kennedy, J. J., Rayner, N. A., and Jones, P. D.: Quantifying uncertainties in global and regional temperature change using an ensemble of observational estimates: The HadCRUT4 data set, J. Geophys. Res., 117, D08101, doi:10.1029/2011JD017187, 2012.

Noilhan, J. and Mahfouf, J.-F.: The ISBA land surface parameterisation scheme, Global Planet. Change, 13, 145–159, doi:10.1016/0921-8181(95)00043-7, 1996.

Noilhan, J. and Planton, S.: A Simple Parameterization of Land Surface Processes for Meteorological Models, Mon. Weather Rev., 117, 536–549, doi:10.1175/1520-0493(1989)117<0536:ASPOLS>2.0.CO;2, 1989.

Oki, T. and Sud, Y. C.: Design of Total Runoff Integrating Pathways (TRIP) – A Global River Channel Network, Earth Interact., 2, 1–36, 1997.

O'Reilly, J. E., Maritorena, S., Mitchell, B. G., Siegel, D. A., Carder, K. L., Garver, S. A., Kahru, M., and McClain, C.: Ocean color chlorophyll algorithms for SeaWiFS, J. Geophys. Res., 103, 24937–24953, doi:10.1029/98JC02160, 1998.

Orsi, A., Johnson, G., and Bullister, J.: Circulation, mixing, and production of Antarctic Bottom Water, Prog. Oceanogr., 43, 55–109, doi:10.1016/S0079-6611(99)00004-X, 1999.

Parton, W. J., Stewart, J. W. B., and Cole, C. V.: Dynamics of C, N, P and S in grassland soils: a model, Biogeochemistry, 5, 109–131, doi:10.1007/BF02180320, 1988.

Pérez, F. F., Mercier, H., Vázquez-Rodríguez, M., Lherminier, P., Velo, A., Pardo, P. C., Rosón, G., and Ríos, A. F.: Atlantic Ocean CO$_2$ uptake reduced by weakening of the meridional overturning circulation, Nat. Geosci., 6, 146–152, doi:10.1038/ngeo1680, 2013.

Piao, S., Sitch, S., Ciais, P., Friedlingstein, P., Peylin, P., Wang, X., Ahlström, A., Anav, A., Canadell, J. G., Cong, N., Huntingford, C., Jung, M., Levis, S., Levy, P. E., Li, J., Lin, X., Lomas, M. R., Lu, M., Luo, Y., Ma, Y., Myneni, R. B., Poulter, B., Sun, Z., Wang, T., Viovy, N., Zaehle, S., and Zeng, N.: Evaluation of terrestrial carbon cycle models for their response to climate variability and to CO$_2$ trends, Global Change Biol., 19, 2117–2132, doi:10.1111/gcb.12187, 2013.

Pinker, R. T. and Laszlo, I.: Modeling Surface Solar Irradiance for Satellite Applications on a Global Scale, J. Appl. Meteorol., 31, 194–211, doi:10.1175/1520-0450(1992)031<0194:MSSIFS>2.0.CO;2, 1992.

Rawlins, M. A., McGuire, A. D., Kimball, J. S., Dass, P., Lawrence, D., Burke, E., Chen, X., Delire, C., Koven, C., MacDougall, A., Peng, S., Rinke, A., Saito, K., Zhang, W., Alkama, R., Bohn, T. J., Ciais, P., Decharme, B., Gouttevin, I., Hajima, T., Ji, D., Krinner, G., Lettenmaier, D. P., Miller, P., Moore, J. C., Smith, B., and Sueyoshi, T.: Assessment of model estimates of land-atmosphere CO_2 exchange across Northern Eurasia, Biogeosciences, 12, 4385–4405, doi:10.5194/bg-12-4385-2015, 2015.

Rayner, N. A., Parker, D. E., Horton, E. B., Folland, C. K., Alexander, L. V., Rowell, D. P., Kent, E. C., and Kaplan, A.: Global analyses of sea surface temperature, sea ice, and night marine air temperature since the late nineteenth century, J. Geophys. Res., 108, 4407, doi:10.1029/2002JD002670, 2003.

Regnier, P., Friedlingstein, P., Ciais, P., Mackenzie, F. T., Gruber, N., Janssens, I. A., Laruelle, G. G., Lauerwald, R., Luyssaert, S., Andersson, A. J., Arndt, S., Arnosti, C., Borges, A. V., Dale, A. W., Gallego-Sala, A., Goddéris, Y., Goossens, N., Hartmann, J., Heinze, C., Ilyina, T., Joos, F., LaRowe, D. E., Leifeld, J., Meysman, F. J. R., Munhoven, G., Raymond, P. A., Spahni, R., Suntharalingam, P., and Thullner, M.: Anthropogenic perturbation of the carbon fluxes from land to ocean, Nat. Geosci, 8, 597–607, doi:10.1038/ngeo1830, 2013.

Running, S. W., Nemani, R. R., Heinsch, F. A., Zhao, M., Reeves, M., and Hashimoto, H.: A Continuous Satellite-Derived Measure of Global Terrestrial Primary Production, BioScience, 54, 547–560, 2004.

Sabine, C., Feely, R., Gruber, N., Key, R., Lee, K., Bullister, J., Wanninkhof, R., Wong, C., Wallace, D., Tilbrook, B., Millero, F., Peng, T., Kozyr, A., Ono, T., and Rios, A.: The oceanic sink for anthropogenic CO(2), Science, 305, 367–371, doi:10.1126/science.1097403, 2004.

Salas y Mélia, D.: A global coupled sea ice–ocean model, Ocean Model., 4, 137–172, doi:10.1016/S1463-5003(01)00015-4, 2002.

Sallée, J., Speer, K., and Rintoul, S. R.: Zonally asymmetric response of the Southern Ocean mixed-layer depth to the Southern Annular Mode, Nat. Geosci., 3, 273–279, doi:10.1038/ngeo812, 2010.

Sallée, J.-B., Matear, R. J., Rintoul, S. R., and Lenton, A.: Localized subduction of anthropogenic carbon dioxide in the Southern Hemisphere oceans, Nat. Geosci., 5, 579–584, doi:10.1038/ngeo1523, 2012.

Sallée, J. B., Shuckburgh, E., Bruneau, N., Meijers, A. J. S., Bracegirdle, T. J., Wang, Z., and Roy, T.: Assessment of Southern Ocean water mass circulation and characteristics in CMIP5 models: Historical bias and forcing response, J. Geophys. Res.-Oceans, 118, 1830–1844, doi:10.1002/jgrc.20135, 2013.

Sander, S. P. , Friedl, R. R., Golden, D. M., Kurylo, M. J., Moortgat, G. K., Keller-Rudek, H., Wine, P. H., Ravishankara, A. R., Kolb, C. E., Molina, M. J., Finlayson-Pitts, B. J., Huie, R. E., and Orkin, V. L.: Chemical Kinetics and Photochemical Data for Use in Atmospheric Studies, JPL Publication 06-2, Evaluation no. 15, Pasadena, California, USA, 2006.

Sarmiento, J. L. and Gruber, N.: Ocean Biogeochemical Dynamics, Princeton University Press, 2006.

Sarrat, C., Noilhan, J., Dolman, A. J., Gerbig, C., Ahmadov, R., Tolk, L. F., Meesters, A. G. C. A., Hutjes, R. W. A., Ter Maat, H. W., Pérez-Landa, G., and Donier, S.: Atmospheric CO_2 modeling at the regional scale: an intercomparison of 5 meso-scale atmospheric models, Biogeosciences, 4, 1115–1126, doi:10.5194/bg-4-1115-2007, 2007.

Schwinger, J., Tjiputra, J. F., Heinze, C., Bopp, L., Christian, J. R., Gehlen, M., Ilyina, T., Jones, C. D., Salas-Mélia, D., Segschneider, J., Séférian, R., and Totterdell, I.: Non-linearity of ocean carbon cycle feedbacks in CMIP5 earth system models, J. Climate, 27, 140310121516000, doi:10.1175/JCLI-D-13-00452.1, 2014.

Séférian, R., Bopp, L., Gehlen, M., Orr, J., Ethé, C., Cadule, P., Aumont, O., Salas y Mélia, D., Voldoire, A., and Madec, G.: Skill assessment of three earth system models with common marine biogeochemistry, Clim. Dynam., 40, 2549–2573, doi:10.1007/s00382-012-1362-8, 2013.

Séférian, R., Ribes, A., and Bopp, L.: Detecting the anthropogenic influences on recent changes in ocean carbon uptake, Geophys. Res. Lett., 2014, GL061223, doi:10.1002/2014GL061223, 2014.

Sheffield, J., Goteti, G., and Wood, E. F.: Development of a 50-Year High-Resolution Global Dataset of Meteorological Forcings for Land Surface Modeling, J. Climate, 19, 3088–3111, doi:10.1175/JCLI3790.1, 2006.

Simmons, H., Jayne, S., St Laurent, L., and Weaver, A.: Tidally driven mixing in a numerical model of the ocean general circulation, Ocean Model., 6, 245–263, doi:10.1016/S1463-5003(03)00011-8, 2004.

Soetaert, K., Middelburg, J., Herman, P., and Buis, K.: On the coupling of benthic and pelagic biogeochemical models, Earth-Sci Rev., 51, 173–201, 2000.

Sunda, W. and Huntsman, S.: Interrelated influence of iron, light and cell size on marine phytoplankton growth, Nature, 390, 389–392, 1997.

Szczypta, C., Decharme, B., Carrer, D., Calvet, J.-C., Lafont, S., Somot, S., Faroux, S., and Martin, E.: Impact of precipitation and land biophysical variables on the simulated discharge of European and Mediterranean rivers, Hydrol. Earth Syst. Sci., 16, 3351–3370, doi:10.5194/hess-16-3351-2012, 2012.

Szczypta, C., Calvet, J.-C., Maignan, F., Dorigo, W., Baret, F., and Ciais, P.: Suitability of modelled and remotely sensed essential climate variables for monitoring Euro-Mediterranean droughts, Geosci. Model Dev., 7, 931–946, doi:10.5194/gmd-7-931-2014, 2014.

Szopa, S., Balkanski, Y., Schulz, M., Bekki, S., Cugnet, D., Fortems-Cheiney, A., Turquety, S., Cozic, A., Déandreis, C., Hauglustaine, D., Idelkadi, A., Lathière, J., Lefèvre, F., Marchand, M., Vuolo, R., Yan, N., and Dufresne, J.-L.: Aerosol and ozone changes as forcing for climate evolution between 1850 and 2100, Clim. Dynam., 40, 2223–2250, doi:10.1007/s00382-012-1408-y, 2013.

Takahashi, T.: Climatological mean and decadal change in surface ocean pCO$_2$, and net sea–air CO_2 flux over the global oceans, Deep Sea Res. Pt. II, 56, 554–577, doi:10.1016/j.dsr2.2008.12.009, 2009.

Takahashi, T., Broecker, W., and Langer, S.: Redfield Ratio Based on Chemical-Data From Isopycnal Surfaces, J. Geophys. Res.-Oceans, 90, 6907–6924, 1985.

Takahashi, T., Sutherland, S. C., and Kozyr, A.: Global Ocean Surface Water Partial Pressure of CO_2 Database: Measurements Performed during 1968–2010 (Version 2010), CDIAC-152, CDIAC-152, ORNL, 2010.

Talley, L. D., Reid, J. L., and Robbins, P. E.: Data-Based Meridional Overturning Streamfunctions for the Global

Ocean, J. Climate, 16, 3213–3226, doi:10.1175/1520-0442(2003)016<3213:DMOSFT>2.0.CO;2, 2003.

Taylor, K. E., Stouffer, R. J., and Meehl, G. A.: A Summary of the CMIP5 Experiment Design, 2009 Edn., International CLIVAR Project Office, 2009.

Tegen, I. and Fung, I.: Contribution to the Atmospheric Mineral Aerosol Load From Land-Surface Modification, J. Geophys. Res.-Atmos., 100, 18707–18726, 1995.

Thorndike, A. S., Rothrock, D. A., Maykut, G. A., and Colony, R.: The thickness distribution of sea ice, J. Geophys. Res., 80, 4501–4513, doi:10.1029/JC080i033p04501, 1975.

Valcke, S.: The OASIS3 coupler: a European climate modelling community software, Geosci. Model Dev., 6, 373–388, doi:10.5194/gmd-6-373-2013, 2013.

Voldoire, A., Sanchez-Gomez, E., Salas y Mélia, D., Decharme, B., Cassou, C., Sénési, S., Valcke, S., Beau, I., Alias, A., Chevallier, M., Déqué, M., Deshayes, J., Douville, H., Fernandez, E., Madec, G., Maisonnave, E., Moine, M. P., Planton, S., Saint-Martin, D., Szopa, S., Tyteca, S., Alkama, R., Belamari, S., Braun, A., Coquart, L., and Chauvin, F.: The CNRM-CM5.1 global climate model: description and basic evaluation, Clim. Dynam., 40, 2091–2121, doi:10.1007/s00382-011-1259-y, 2013.

Wanninkhof, R.: A relationship between wind speed and gas exchange over the ocean, J. Geophys. Res., 97, 7373–7382, 1992.

Wanninkhof, R., Park, G. -H., Takahashi, T., Sweeney, C., Feely, R., Nojiri, Y., Gruber, N., Doney, S. C., McKinley, G. A., Lenton, A., Le Quéré, C., Heinze, C., Schwinger, J., Graven, H., and Khatiwala, S.: Global ocean carbon uptake: magnitude, variability and trends, Biogeosciences, 10, 1983–2000, doi:10.5194/bg-10-1983-2013, 2013.

Wassmann, P., Duarte, C. M., Agustí, S., and Sejr, M. K.: Footprints of climate change in the Arctic marine ecosystem, Glob. Change Biol., 17, 1235–1249, doi:10.1111/j.1365-2486.2010.02311.x, 2010.

Watanabe, M., Kamae, Y., Yoshimori, M., Oka, A., Sato, M., Ishii, M., Mochizuki, T., and Kimoto, M.: Strengthening of ocean heat uptake efficiency associated with the recent climate hiatus, Geophys. Res. Lett., 40, 3175–3179, doi:10.1002/grl.50541, 2013.

Wenzel, S., Cox, P. M., Eyring, V., and Friedlingstein, P.: Emergent constraints on climate-carbon cycle feedbacks in the CMIP5 Earth system models, J. Geophys. Res.-Biogeo., 2013, JG002591, doi:10.1002/2013JG002591, 2014.

Wetzel, P., Maier-Reimer, E., Botzet, M., Jungclaus, J., Keenlyside, N., and Latif, M.: Effects of ocean biology on the penetrative radiation in a coupled climate model, J. Climate, 19, 3973–3988, 2006.

Willis, J. K., Roemmich, D., and Cornuelle, B.: Interannual variability in upper ocean heat content, temperature, and thermosteric expansion on global scales, J. Geophys. Res., 109, C12036, doi:10.1029/2003JC002260, 2004.

Yin, X.: Responses of leaf nitrogen concentration and specific leaf area to atmospheric CO_2 enrichment: a retrospective synthesis across 62 species, Glob. Change Biol., 8, 631–642, doi:10.1046/j.1365-2486.2002.00497.x, 2002.

Zhu, Z., Bi, J., Pan, Y., Ganguly, S., Anav, A., Xu, L., Samanta, A., Piao, S., Nemani, R., and Myneni, R.: Global Data Sets of Vegetation Leaf Area Index (LAI)3g and Fraction of Photosynthetically Active Radiation (FPAR)3g Derived from Global Inventory Modeling and Mapping Studies (GIMMS) Normalized Difference Vegetation Index (NDVI3g) for the Period 1981 to 2011, Remote Sensing, 5, 927–948, doi:10.3390/rs5020927, 2013.